

POLITECNICO DI TORINO

Faculty of Aerospace Engineering

Master Thesis

**Flexible Spacecraft Modelling and
Control with a Robotic
Manipulator**



Supervisor

Dr. Elisa Capello

Co-supervisor:

Dr. Mauro Mancini

Candidate:

Pierangela Morga

April 2021

To my family.

Acknowledgements

I would like to thank my supervisors Dr. Elisa Capello and Dr. Mauro Mancini for their help and constant presence during all the period of the thesis, despite the distance and the difficult times.

Abstract

The growing of space debris orbiting around the Earth has become a significant problem for active spacecraft and future missions, due to the risk of collision and the accumulation of artificial objects, especially in Low Earth Orbit (LEO). In order to mitigate the problem, new solutions have been proposed. Space robotics has been included in on-orbit services to help human activities in the space environment, and in particular robotic manipulators can play a key role in active debris removal. The purpose of this thesis is the development of a flexible spacecraft dynamics and control model including a space manipulator. A hybrid approach is used for implementing the main body and the manipulator dynamics. In particular, the manipulator equations of motion are obtained from Lagrangian formulation, while the main body dynamics is expressed with Euler equations for a rigid body. The robotic arm is a two Degrees Of Freedom (DOF) planar manipulator with two links. The main structural properties are chosen after a comparison of space robotic arms from literature. On the other hand, the JAXA micro-satellite PROximate Object Close flyby with Optical Navigation (PROCYON) is used as the main body of the spacecraft. As in PROCYON spacecraft, a system of four reaction wheels in pyramidal configuration is considered. All modelling and simulation phases are made in MATLAB/SIMULINK environment.

Another important aspect of this work is the flexible part of the satellite, represented by the four solar panels of PROCYON spacecraft. A Finite Element Method (FEM) analysis with PATRAN/NASTRAN is conducted to obtain the natural modes and frequencies necessary for the model and a coupling matrix between rigid and flexible part is also evaluated.

The second part of the thesis is about control strategies. Two different controllers are used for the movement of the manipulator and the main body attitude control. A simple Proportional-Integral-Derivative (PID) controller is implemented for the robotic arm, with the purpose of achieving the desired joint angle position for debris/target capture. For attitude control, an Active Disturbance Rejection Control (ADRC) with a Linear Quadratic Regulator (LQR) as control law is used, in order to obtain a fast and stable response with the rejection of all internal and external disturbances acting on the system. The satisfactory results in the simulation environment demonstrate the capability of the ADRC to perform attitude control,

although the high disturbance due to the manipulator movement and the vibrations of the solar panels. The PID itself ensures good performance and allows to obtain a stable response of the manipulator.

Contents

List of Figures	VIII
List of Tables	X
1 Introduction	1
1.1 Space missions with manipulators	2
1.1.1 Space Shuttle Remote Manipulator System	3
1.1.2 ISS manipulator systems	5
1.1.3 ROTEX	7
1.1.4 ETS-VII	8
1.1.5 Orbital Express	8
1.1.6 SUMO	8
1.2 Space debris mitigation	10
1.2.1 Active debris removal technologies	11
1.2.2 Space debris removal missions	12
1.3 Goals of the work	15
1.4 Overview of the thesis	17
2 System mathematical model	18
2.1 Attitude kinematics and dynamics	19
2.1.1 Attitude kinematics	19
2.1.2 Attitude dynamics	20
2.1.3 State-space equation	24
2.2 Space manipulator	26
2.2.1 Lagrangian Equations	26
2.2.2 Dynamics of the two-link planar manipulator	27
2.3 Flexible Spacecraft	30
2.3.1 Flexible Spacecraft Dynamics	31
2.3.2 Coupling matrix	33
2.3.3 FEM analysis	38

3	Controllers	41
3.1	PID Controller	41
3.1.1	Robotic arm control	43
3.2	Attitude control	43
3.2.1	ADRC	43
3.2.2	ADRC/LQR for attitude control	48
4	Simulation results	50
4.1	Overview of the mission	50
4.2	Simulation environment	52
4.3	Robotic manipulator results	53
4.4	Flexible solar panels results	54
4.4.1	FEM analysis results	54
4.4.2	Solar panels simulation results	56
4.5	Attitude control results	58
4.5.1	Attitude control without the manipulator movement	58
4.5.2	Attitude control with the manipulator movement	60
4.5.3	ADRC/LQR parameters tuning	62
4.5.4	Comparison of ADRC/LQR and LQR controllers	65
4.6	CAD model and animations	68
5	Conclusions and future works	70
	References	72

List of Figures

1.1	Space robots typology	2
1.2	Space Shuttle Remote Manipulator System [12].	3
1.3	SRMS arm assembly [13].	4
1.4	An astronaut anchored to the end of the Canadarm is being lifted up to the top of the Hubble telescope to install protective covers on the satellite [15].	4
1.5	ISS-Mounted Manipulator Systems	6
1.6	The Robotic Refueling Mission (RRM) investigation uses the International Space Station’s Canadarm2 and the Canadian Dextre robot (right) to demonstrate satellite-servicing tasks [20].	6
1.7	CubeSat deploy from NRCSD at tip of JEMRMS [22].	7
1.8	European Robotic Arm [24].	7
1.9	Space robot technology.	9
1.10	Space debris problem [32].	10
1.11	Contact technologies for debris capture	12
1.12	ESA’s e.Deorbit mission	13
1.13	VESPA removal with Clearspace-1 illustration [49].	14
1.14	DEOS demonstration mission [52].	14
1.15	N1 to N4: net experiment, V1 to V3: vision-based navigation experiment, H1 to H4: harpoon experiment, D1 to D3: dragsail experiment [55].	15
1.16	Attitude GNC system.	16
2.1	The scheme of flexible spacecraft with robotic arm and solar panels.	18
2.2	PROCYON top and bottom views (Image credits: JAXA/UT).	19
2.3	Reaction wheels model.	21
2.4	Reaction wheels pyramidal configuration.	22
2.5	2 DOF planar manipulator scheme [67].	27
2.6	Revolute joint [68].	28
2.7	Flexible spacecraft appendages [72].	31
2.8	Solar panels of PROCYON spacecraft [73].	31
2.9	Discrete-parameter appendage sub-body coordinates [76].	34

2.10	Front and upper view of spacecraft with sub-panels division.	35
2.11	Solar panels reference frames.	37
2.12	Solar panels model on Patran.	38
2.13	First six modes of a solar panel fixed to a satellite [77].	39
2.14	Real eigenvectors/eigenvalues from natural frequency analysis [79].	40
3.1	Block diagram of a PID controller.	42
3.2	Block diagram of the robotic manipulator PID controller	43
3.3	Traditional ADRC configuration	44
3.4	ESO input and output	46
3.5	Block diagram of LQR optimal controller	48
3.6	Block diagram of ADRC/LQR for attitude control	48
4.1	Spacecraft block scheme in Simulink	52
4.2	Robotic manipulator motion	53
4.3	Robotic manipulator actuators toques	53
4.4	Mode 1.	55
4.5	Mode 2.	55
4.6	Mode 3.	56
4.7	Solar panels disturbance torque	57
4.8	Solar panels disturbance torque during an attitude manoeuvre	58
4.9	Quaternions response without the manipulator disturbance	59
4.10	Euler angles without the manipulator disturbance	59
4.11	Angular velocity without the manipulator disturbance	59
4.12	RWs torque commands without the manipulator disturbance	60
4.13	Gravity gradient torque	60
4.14	Quaternions response with the manipulator disturbance	61
4.15	Euler angles with the manipulator disturbance	61
4.16	Angular velocity with the manipulator disturbance	62
4.17	RWs torque commands with the manipulator disturbance	62
4.18	Estimation of Euler angles with ESO.	63
4.19	Estimation of Euler angles derivatives with ESO.	64
4.20	Estimation of total disturbance f with ESO.	64
4.21	Comparison of q_0	66
4.22	Comparison of q_1	66
4.23	Comparison of q_2	66
4.24	Comparison of q_3	67
4.25	Comparison of ϕ	67
4.26	Comparison of θ	67
4.27	Comparison of ψ	68
4.28	VR Sink block graphics interface.	68
4.29	Spacecraft CAD model	69

List of Tables

3.1	PID gains	42
4.1	Mission specifications	51
4.2	Actuators specifications	51
4.3	PID controller gains	54
4.4	PID controller gains	54
4.5	Parameters of ADRC	63
4.6	Resulting time responses of ADRC/LQR and LQR	65

Chapter 1

Introduction

Space robotics has a relevant role in space missions and explorations. There are several activities that space robots can do to help human exploration, such as assembly and maintenance of large structures in Earth's orbit, sampling on outer planets surfaces, space debris removal, or assistance for astronauts. All of these tasks represent a hard challenge for humans and robotics can provide greater access beyond human limitations in the harsh environment of space [1]. In order to have a classification, as in [1], space robots can be divided in orbital robots and planetary robots. Orbital robots (Fig. 1.1) are used for repairing satellites, assembling large structures as telescopes, capturing and returning asteroids, deployment of instruments for scientific investigations. On the other hand, planetary robots (Fig. 1.1) play a key role in all the activities involved in the exploration of extraterrestrial surfaces, such as planets or natural satellites.

This thesis aims at developing a flexible spacecraft dynamics and control model, including a robotic manipulator and four solar panels. The 50 kg-class micro-satellite PROCYON developed by JAXA is chosen as the main body of the spacecraft. The attention is focused on the robotic manipulator that can be used to capture a target. The target can be represented by a collaborative spacecraft, as for a docking manoeuvre, but also by a non-collaborative object, as in the case of a space debris. In recent years, lots of space agencies have got more involved in this problem and they are looking for new solutions in order to manage the space junk issue and minimize collisions in space [2].

In this introduction two different topics are discussed:

- Generic space missions with a robotic manipulator.
- Space debris mitigation.

Firstly, an historical overview about space robots with their multiple applications is argued. In particular, the main focus of the discussion is on space missions

including manipulators. In the second part, a brief review about space debris problem and robotic arms used for debris removal is presented. In addition, a section is dedicated to the scope of the thesis in terms of the control strategies adopted for the attitude control, included in the Guidance, Navigation and Control (GNC) system. Finally, an overview of the work is presented in order to provide a brief description of all the parts of the thesis.

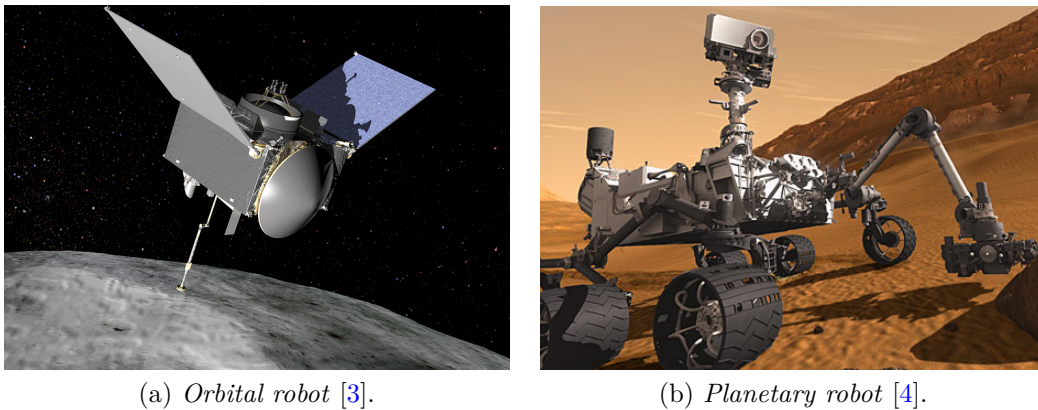


Figure 1.1: Space robots typology

1.1 Space missions with manipulators

The manipulators are robotic arms that are used for space operation, assembly and servicing [5]. Robotic On-Orbit Service (OOS) is a class of mission in which a robotic servicer (chaser) spacecraft intercepts and performs servicing tasks on a client (target) spacecraft [6]. OOS comprises all aspects of on-orbit assembly of parts into systems, maintenance of equipment, replenishment of consumables, upgrade, repair, and target capture and removal. Over more than a decade, numerous projects around the world have dealt with OOS of spacecraft supported by space robotics. A major subset of OOS consists of unmanned OOS missions that use a space robot. [7].

As early as the 1980s, the National Aeronautics and Space Administration (NASA) realized the importance of robotics on-orbit servicing operations. The first robotic arm used in a space mission was the Space Shuttle Remote Manipulator System [8]. After that, other two manipulators followed, Space Station Remote Manipulator System (SSRMS) and Special Purpose Dexterous Manipulator (SPDM). These three manipulators are of special importance due to its size and design complexity [5]. Moreover, space manipulator robotics has played a significant role on the International Space Station (ISS) [6], with three manipulator systems: the Canadian

Mobile Servicing System (MSS), that includes the SSRMS and SPDM mentioned before, the Japanese Experiment Module Remote Manipulator System (JEMRMS), and the European Robotic Arm (ERA). There have been several technology demonstrator missions beginning with the foundational ETS-VII mission [6], such as ROTEX and DARPA program. In the following sections a brief description of some of the most important applications of space manipulators in past and current space missions is presented.

1.1.1 Space Shuttle Remote Manipulator System

Developed by the Canadian Space Agency (CSA) [9], the Shuttle Remote Manipulator System (SRMS) (fig. 1.2), also called as Canadarm, is a mechanical arm that manoeuvres a payload from the payload bay of the Space Shuttle orbiter to its deployment position and then releases it [8]. It can also grapple a free-flying payload and berth it to the payload bay of the orbiter. The SRMS comprises a 6 degree-of-freedom, 15.2 m long arm attached to the port longeron of the shuttle orbiter cargo bay, a display and control system and the payload interface, as shown in Fig. 1.3. Control of the arm is effected by the use of hand controllers, a dedicated RMS display and control panel, and CRT monitors located in the orbiter crew compartment. This is augmented by the orbiter CCTV monitors, and General Purpose Computer (GPC). From the point where the RMS is attached to the Orbiter, the arm is comprised of 2 single degree-of-freedom shoulder joints (shoulder yaw and shoulder pitch), a 21 ft. long upper boom, an elbow (pitch) joint, a 23 ft. long lower boom, 3 single degree-of-freedom wrist joints (wrist pitch, wrist yaw and wrist roll), and a snare end effector which interfaces with a grapple fixture mounted to the payload [10, 11].



Figure 1.2: Space Shuttle Remote Manipulator System [12].

The first test in orbit of Canadarm was done in 1981, on Space Shuttle Columbia's

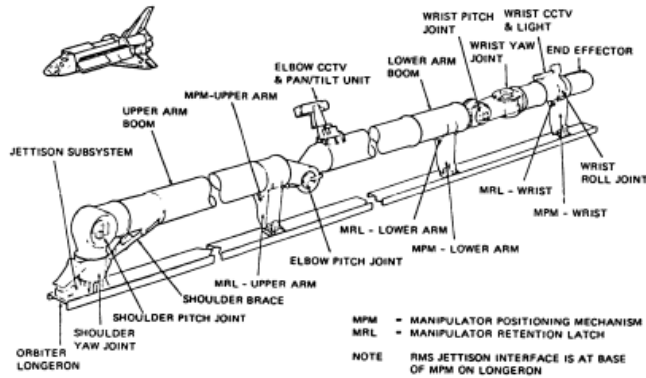


Figure 1.3: SRMS arm assembly [13].

STS-2 mission, while the first operational mission of the arm was on STS-3 to deploy and manoeuvre the Plasma Diagnostics Package [14]. The main tasks of SRMS in Space Shuttle flight missions were payload deployment or berthing, and also astronauts assistance in Extra-Vehicular Activities (EVAs). The cooperative use of SRMS and human EVAs allowed spacewalks, maintenance missions, such as the repair of the Hubble space telescope (Fig. 1.4), and construction tasks of the International Space Station have also been successfully, as the connection of the first two modules [8].



Figure 1.4: An astronaut anchored to the end of the Canadarm is being lifted up to the top of the Hubble telescope to install protective covers on the satellite [15].

1.1.2 ISS manipulator systems

The International Space Station (ISS) is the largest international technology project, with 15 countries making significant cooperative contributions [8]. In order to facilitate various activities on the station, there are several robotic systems.

Space station remote manipulator system

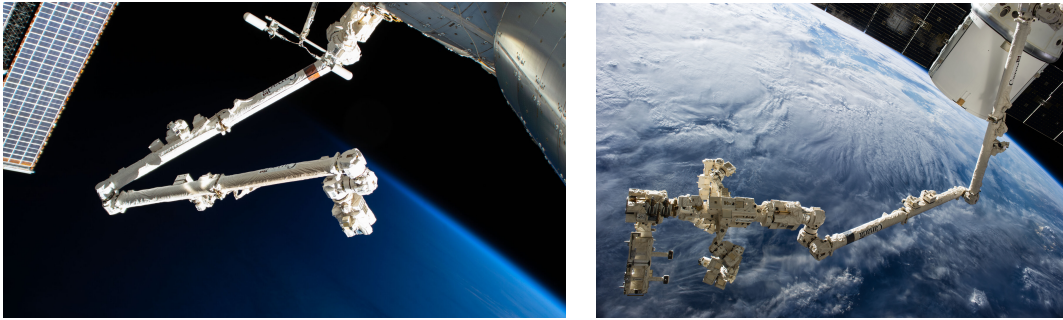
The Space Station Remote Manipulator System (SSRMS), also known as *Canadarm2* (Fig. 1.5), has been successfully installed on-orbit, checked-out during STS-100 in April 2001, and performed its first Space Station assembly task during STS-104 in July 2001 [16]. The arm is 17.6 m long when fully extended and has seven degrees of freedom [17]. SSRMS can be placed on the Mobile Base System (MBS) attached to the structure of ISS. This component has 1 DOF and can work jointly with SSRMS [5]. The arm has several applications on the ISS: in addition to move itself around the station, the Canadarm2 can use a grapple fixture to move any object or large segments into the required place on the space station. It also can be used to capture and dock cargo spacecraft like the SpaceX Dragon, the Cygnus spacecraft and Japanese H-II Transfer Vehicle (HTV), and to undock and release them after use.

Special Purpose Dexterous Manipulator

The Special Purpose Dexterous Manipulator (SPDM), also known as *Dextre* (Fig. 1.5), was launched on March 2008. As reported in [8], the SPDM is a dual-arm manipulator system, where each manipulator has seven degrees of freedom and is mounted on a one-degrees-of-freedom body joint. Its primary function is the change-out of small equipment on the Space Station's exterior. Other SPDM tasks include scientific payload servicing, inspection and monitoring in support of extravehicular activities. The SPDM can either be operated from the end of the SSRMS (see Fig. 1.6) or as a stand-alone manipulator system. This is an example of multi-arms cooperation [9]: two arms can work together to achieve difficult tasks that would be otherwise impossible to complete with only a single arm. This occurred on April 28, 2001 when SSRMS transferred a piece of equipment over to SRMS. This event is known as the *handshake in space* of the two Canadian robotic arms.

Japanese Experiment Module Remote Manipulator System

The Japanese Experiment Module Remote Manipulator System (JEMRMS) (fig. 1.7), built by the Japan Aerospace Exploration Agency (JAXA), is a robotic manipulator system intended for supporting experiments conducted on the Exposed Facility (EF) of the Japanese Experiment Module (JEM) [21]. This robot includes



(a) *Space station remote manipular system* [18]. (b) *Special Purpose Dexterous Manipulator* [19].

Figure 1.5: ISS-Mounted Manipulator Systems



Figure 1.6: The Robotic Refueling Mission (RRM) investigation uses the International Space Station's Canadarm2 and the Canadian Dextre robot (right) to demonstrate satellite-servicing tasks [20].

a 6-DOF, 10 m long main arm, and a 6-DOF, 2 m long Small Fine Arm (SFA) designed to perform dexterous tasks [9]. The arm can be used to handle and relocate the components for the experiments and observations on the exposed facility [8].

European Robotic Arm

In March 1996 European Space Agency (ESA) signed a contract with Fokker Space on the full scale development of the European Robotic Arm (ERA)(Fig. 1.8), that represents a co-operative development with the Russian Space Agency used to assemble and service the Russian Segment of the International Space Station [23]. ERA is a 11 m long manipulator with 7-DOF, two booms and a re-allocable base to be attached to the Russian segment of the ISS [9]. It will be the first robot arm able to work on the Russian space station segments under its own control, performing many tasks automatically or semi-automatically. Specific application of ERA



Figure 1.7: CubeSat deploy from NRCSD at tip of JEMRMS [22].

include installation, deployment and replacement of solar arrays, inspection of the ISS, handling of external payloads and astronauts' assistance during space walks.

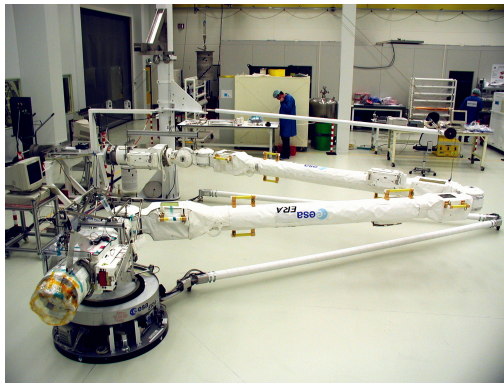


Figure 1.8: European Robotic Arm [24].

1.1.3 ROTEX

The German Robot Technology EXperiment (ROTEX) is one of the milestones of space robot technology [7] (Fig. 1.9). ROTEX was developed by German Aerospace Agency (DRL). A multi-sensory robotic arm was flown on the Space Shuttle Columbia in 1993 [8], and it was operated by an on-board astronaut and an operator from ground. ROTEX was the first remotely controlled robot in space, and several key technologies were successfully tested, such as a multi-sensor gripper, tele-operation from the ground, shared autonomy, and time-delay compensation by a predictive 3D-stereo-graphic display [25].

1.1.4 ETS-VII

Another important milestone in the development of space robot technology and the first robotic OOS demonstration mission is the Japanese Engineering Test Satellite VII (ETS-VII), shown in Fig. 1.9. It was an unmanned spacecraft developed and launched by the *National Space Development Agency of Japan* (NASDA, currently JAXA) in 1997 [8]. ETS-VII system consists of two satellites: the chaser and the target [26]. A 2-m long is installed on the chaser satellite, providing a 6 DOF manoeuvring capability [27]. The objective of the ETS-VII mission is to verify technologies for autonomous rendezvous, and docking and robotic servicing in space. These technologies include teleoperation from the ground with a time-delay, robotic servicing task demonstrations, such as deployment of a space structure, dynamically coordinated control between the manipulator's reaction and the satellite's response, and capture and berthing of a target satellite [7].

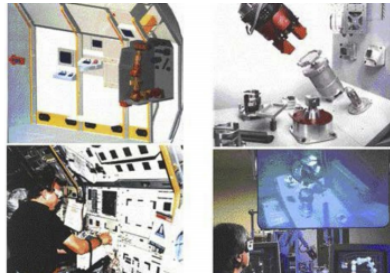
1.1.5 Orbital Express

The Orbital Express space operations architecture program is a Defense Advanced Research Project Agency (DARPA) program developed to validate the technical feasibility of robotic on-orbit refueling and reconfiguration of satellites, as well as autonomous rendezvous, docking, and manipulator berthing [8]. The Orbital Express was successfully launched and accomplished in 2007. The system consists of two satellites (Fig. 1.9): the Autonomous Space Transport & Robotic Orbital servicer (ASTRO) spacecraft, developed by Boeing, and the NextSat, a client satellite provided by Ball Aerospace [28]. A 6 DOF rotary joint robotic arm is mounted on the ASTRO vehicle and is used to capture and service the NextSat. As an advanced OOS technology demonstration mission, the Orbital Express mission demonstrated autonomous capture of a fully unconstrained free-flying client satellite, autonomous transfer of a functional battery On-Orbit Replaceable Unit (ORU) between two spacecraft, and autonomous transfer of a functional computer ORU. These operations were executed as part of a mission scenarios that demonstrated complete sequences of autonomous rendezvous, capture, berthing and ORU transfer.

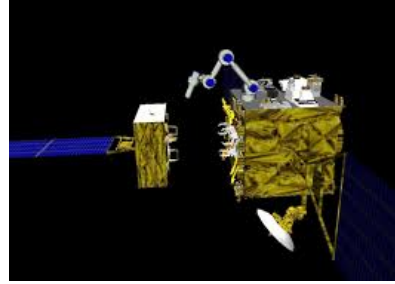
1.1.6 SUMO

Another DARPA OOS program was the Spacecraft of the Universal Modification of Orbits (SUMO)(Fig. 1.9), executed by the NRL (Naval Research Laboratory) in 2002 [9]. The program aimed at combining a detailed stereo photo-grammetric imaging with robotic manipulators to grapple space objects of an existing spacecraft for servicing. In 2005, the program was renamed to Front-end Robotics Enabling Near.term Demonstration (FRIEND), which included a 7-DOF flight manipulator with the objective of performing autonomous rendezvous and docking with satellites not pre-designed for servicing [7]. The FRIEND robotic arm was used in a new

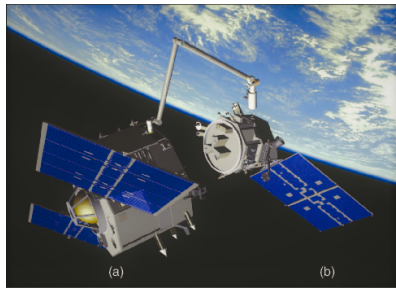
DARPA's Phoenix program in 2012, with the objective of removal and reuse of some existing parts of decommissioned satellites in (Geostationary Earth Orbit) GEO. Moreover, another goal of the Phoenix program was to demonstrate the ability to create new space systems at greatly reduced cost [29].



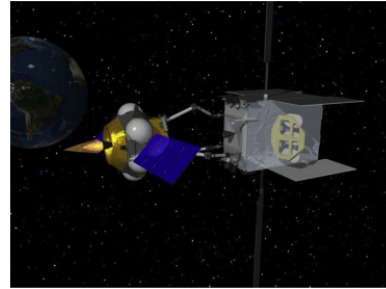
(a) ROTEX manipulator arm [8].



(b) ETS-VII [7].



(c) Orbital Express: (a) ASTRO and (b) NextSat [30].



(d) SUMO [7].

Figure 1.9: Space robot technology.

1.2 Space debris mitigation

Since the launch of Sputnik-1 in 1957 the number of human-made objects in space has been constantly increasing [31] (Fig. 1.10). After that, the North American Aerospace Defence Command (NORAD) began compiling a database (the *Space Object Catalog*) of all known rocket launches and objects in orbit around the Earth, such as satellites, protective shields and upper-stages of launch vehicles.

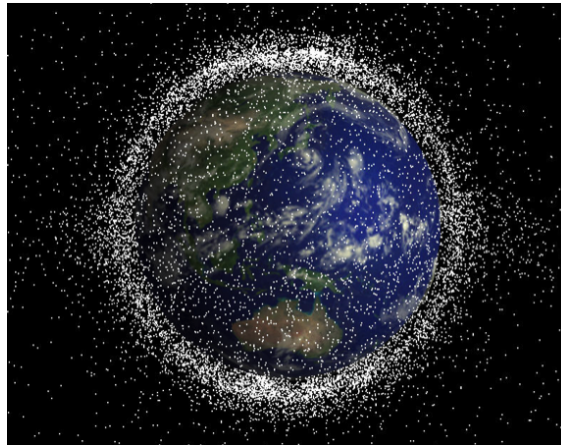


Figure 1.10: Space debris problem [32].

Collisions at orbital velocity represent a highly hazard for functional satellites and can produce even more space debris after the impact [30]. In 2019, the US Space Surveillance Network reported nearly 20,000 artificial objects in orbit above the Earth, including 2,218 operational satellites [33, 34]. All the objects classified as space debris include non-operational satellites, derelict launch vehicle stages, mission-related hardware and fragments resulting from explosions or collisions [31]. In particular, two recent events have greatly worsen the situation:

- In 2007, a Chinese anti-satellite test used a missile to destroy the old meteorological satellite Fengyun FY-1C, and generated 2400 debris pieces larger than 10 cm and 35,000 pieces below the resolution limit at 860 km altitude, increasing the space debris population by 30% [6].
- In 2009, a defunct Russian satellite collided with and destroyed a functioning U.S. Iridium 33 commercial satellite and the decommissioned Cosmos 2251. The collision added more than 2,000 pieces of debris [35] at 790 km altitude.

After these events, the Space Shuttle and ISS increased the numbers of warnings and avoidance collision manoeuvres [30]. For example, the ISS was manoeuvred into

a 1 km higher orbit in 2001 to avoid collision with Russian SL-8 upper stage [6]. The most densely populated region in terms of number of objects in orbit is the Low Earth Orbit (LEO) region, extending from the beginning of the space environment up to an altitude of 2000 km. Below 800 km of altitude, the dominant presence of atmospheric drag ensures a low orbital decay, while at altitudes above the levels where atmospheric drag is significant, the time required for orbital decay is quite long, and these objects can remain in orbit for centuries or millennia [31]. In particular, the LEO population at 800-1000 km sun-synchronous polar orbits around $86 - 110^\circ$ inclination are close to the *Kessler limit*, which is expected to be reached by 2055 [6]. The *Kessler limit* is the point beyond which the debris population becomes self-perpetuating and grows uncontrollably [36]. Simulations have demonstrated that even if the orbital debris population remains as it is today with no further objects added to space, the level of fragmentation in LEO will continue to escalate exponentially [37, 38]. The only way to mitigate this problem is to actively reduce the mass of debris in orbit [31].

1.2.1 Active debris removal technologies

Debris mitigation is a role to which robotic on-orbit servicers can naturally adapt themselves. Indeed, robotic capture is the most controllable approach in which the debris is captured, manoeuvred to a lower orbit (LEO) or graveyard orbit (GEO) and/or a de-orbit device [6]. Many high-level studies on Active Debris Removal (ADR) have been conducted to characterize the types of systems required to capture and remove hazardous debris objects. There are two types of technologies: contact and non-contact [39]. Contact methods (Fig. 1.11) require a physical contact between the chaser spacecraft and the target debris object, while non-contact methods operate at distance. As reported in [39], popular contact technologies include:

- Robotic manipulators: manipulators have been used in several on-orbit tasks, hence are characterized by a high Technology Readiness Levels (TRL).
- Throw-nets: these technologies are deployed from a canister and used to enveloped the target. After that, the debris object can be pulled by a tether attached to the chaser.
- Harpoons: harpoons are fired to attach to the target. The chaser is then able to pull the target using a tether.

Some of non-contact methods mentioned in [39] include:

- Ion-Beam Shepherd (IBS): Ibs employs ions generated by electric propulsion on-board the chaser to exert a force on the target and re-orbit or de-orbit it.
- Electromagnetic forcing: EM forces are generated on the target using electric/-magnetic fields in order to de-orbiting, re-orbiting or de-tumbling the target.
- Laser ablation: lasers are employed to ablate the surface of the target and generate a small but continuous resulting force on it.



(a) A chaser spacecraft approaching a tumbling rocket body debris target using a gripper arm [40].



(b) Harpoon technology [41].

Figure 1.11: Contact technologies for debris capture

1.2.2 Space debris removal missions

Space debris mitigation alone is therefore non sufficient, and it is necessary to introduce a program that is actively involved in space debris problem [42]. The name of this program is Active Debris Removal (ADR), and some agencies like ESA and NASA are conducting studies in order to find new solutions and strategies to stabilize the growth of space debris. In this section, some of the current and future missions and initiatives focused on ADR are presented, especially those with a robotic manipulator.

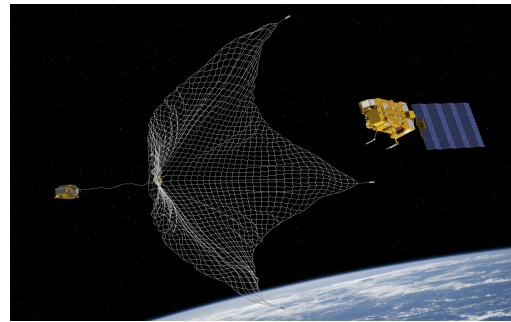
ESA's e.Deorbit mission

ESA is actively working to support the guidelines for the long-term sustainability of outer space activities from the UN Committee on the Peaceful Uses of Outer

Space (COPUOS) [43, 44]. The e.Deorbit mission, being developed through ESA’s Clean Space initiative and scheduled to be launched in 2024, was going to be the first ADR mission conducted by ESA. This mission aimed at removing a large ESA-owned space debris (Envisat) from its current orbit in LEO and performing a controlled re-entry into the atmosphere [42]. The baseline capture method is a robotic arm (Fig. 1.12) for the derelict satellite’s catching, and additional capture method technologies were investigated, including a net and a harpoon [45] (Fig. 1.12).



(a) *e.Deorbit robotic arm concept* [45].



(b) *e.Deorbit system study for ADR - capturing the satellite in a net attached to a tether* [46].

Figure 1.12: ESA’s e.Deorbit mission

Unfortunately, funding of the mission stopped in 2018 [47]. After that, ESA member states got involved in Clear Space One mission (figure 1.13), the follow-up of e.Deorbit. This mission aims at using e.Deorbit’s tentacles option to capture the Vega Secondary Payload Adapter from 2013 Vega flight VV02 for de-orbiting [48].

DEOS mission

Deutsche Orbital Servicing Mission (DEOS) is a on-orbit servicing satellite concept developed by DLR Space Administration from 2012. DEOS consisted of two satellites, a ‘client’ and a ‘servicer’ (Fig. 1.14). Main goals of the mission were capturing a tumbling non-cooperative satellite using a manipulator mounted on a free-flying service-satellite, demonstrating a servicing application and de-orbiting the capture satellite within a pre-defined re-entry corridor [50]. According to planning, DEOS was to be ready for launch in 2018, but the project was cancelled after the definition phase [51].

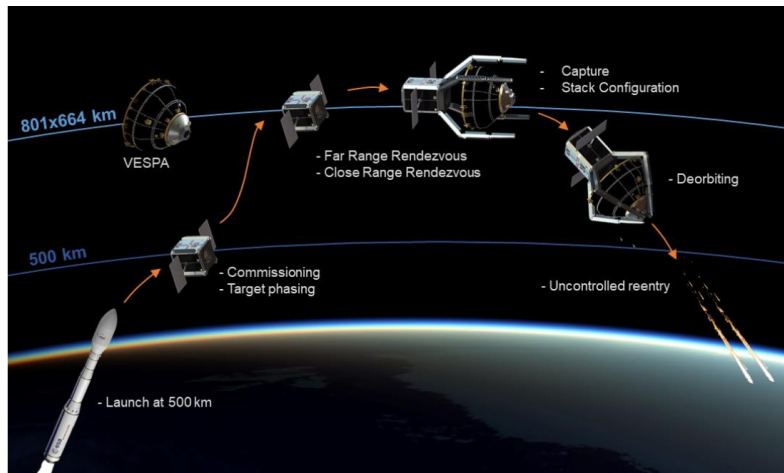


Figure 1.13: VESPA removal with ClearSpace-1 illustration [49].

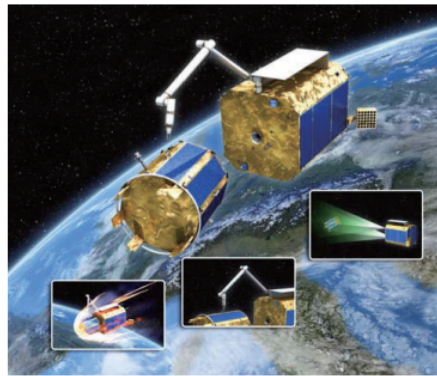


Figure 1.14: DEOS demonstration mission [52].

RemoveDebris

RemoveDEBRIS is a low cost mission aiming to perform key active debris removal technology demonstrations including the use of a net, a harpoon, vision-based navigation and a dragsail in a realistic space operational environment [53]. The core concept behind the mission, is to use a small-satellite as a ‘mothership’, on which the payloads are carried, and from which CubeSats are released and used as ‘pseudo-debris’ targets [54]. The craft was launched to the ISS on the 2nd of April 2018, on board a Dragon capsule. In the following years, the in orbit demonstration were successfully done, in particular the demonstrations of the Net and Harpoon target technologies have confirmed that these are indeed viable technologies for the removal of large space debris [55] (Fig. 1.15). Hence, The RemoveDebris mission has been the first ADR mission to give in orbit demonstrations of cost effective technologies that can be used to observe, capture and dispose of space debris.

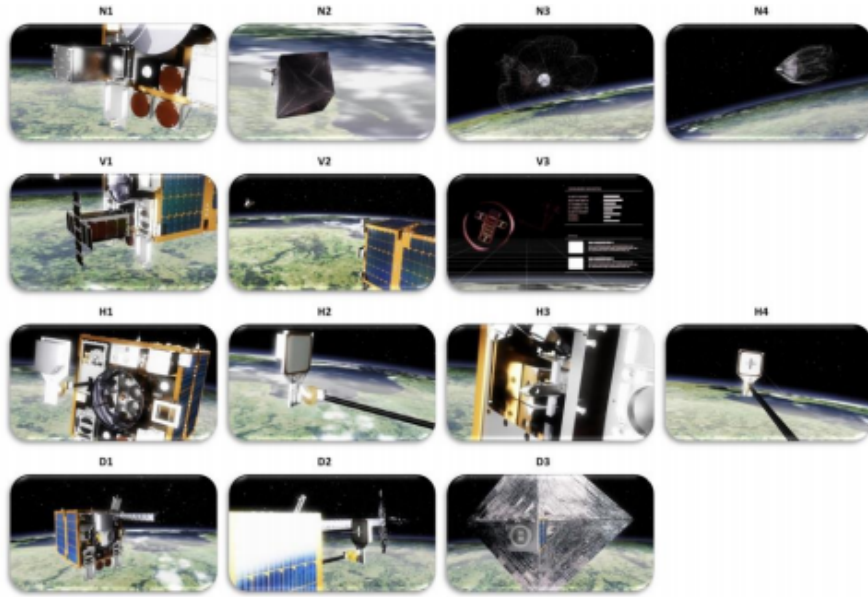


Figure 1.15: N1 to N4: net experiment, V1 to V3: vision-based navigation experiment, H1 to H4: harpoon experiment, D1 to D3: dragsail experiment [55].

1.3 Goals of the work

The scope of this thesis is the development of a simulation model where the Guidance, Navigation and Control (GNC) of a flexible spacecraft is performed. In general, a GNC system consists of three main parts (Fig. 1.16) [56]:

- Guidance: provides at each point the reference values for the state vector in time, that is then compared with the estimated actual values, provided by the navigation function.
- Navigation: consists of a Kalman filter, which provides the controller and the guidance functions with the necessary information on the actual state of the spacecraft.
- Control: provides the force and torque commands necessary to achieve the desired corrections in attitude and trajectory.

The GNC system includes both the components used for position determination and the components used by the Attitude Determination and Control System (ADCS) [57]. The ADCS part includes all the sensors for the attitude determination, such as star trackers, sun sensors, horizon sensors, magnetometers, and gyros. The controller provides the torque required to correct the attitude of the spacecraft, knowing the attitude error between the reference signal and the actual signal from the sensors. This torque is the input of the actuator system, that can include

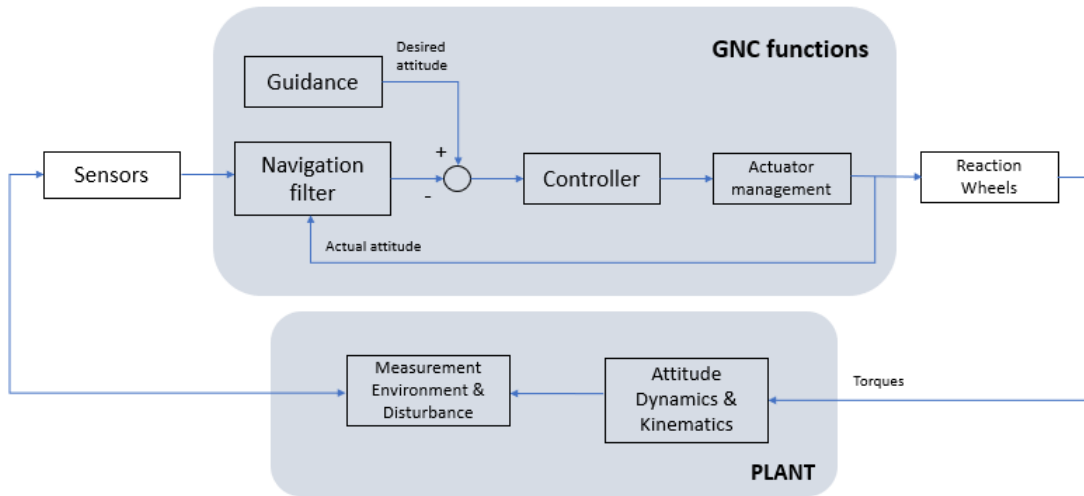


Figure 1.16: Attitude GNC system.

thrusters, reaction wheels, and magnetic torquers. In this work, the navigation system is not studied, and the actual state informations are given by the plant of the system, defined by the attitude kinematics and dynamics. Moreover, the actuator system is represented by the reaction wheels, and the attention is focused on the control part of the ADCS system. This thesis aims at using a combination of two control strategies for the achievement and maintenance of the desired attitude of the spacecraft: the Linear Quadratic Regulator (LQR) and an Active Disturbance Rejection Control (ADRC). This choice is due to the need for a more efficient rejection of all the external and internal disturbances, together with an optimized response of the controller. In fact, the higher value of the robotic arm's disturbance, compared with other external and internal disturbances, justifies the choice of these two controllers. The LQR is recurrent in spacecraft control algorithms, due to the achievement of an optimal behaviour, as can be seen in [58, 59]. The innovative aspect of this thesis is the use of the ADRC combined with the LQR for the attitude control. As reported in [60], the study of an ADRC strategy for the attitude control is advantageous in terms of the disturbance rejection capability. Traditional PID regulator is indeed too simple to obtain high attitude performance, while modern control technologies, such as adaptive control, genetic algorithms and neural network are too complicated to apply in practical applications [60]. ADRC has the properties of inherent robustness, good disturbance rejection and simple design form which make it applicable in aerospace engineering field, as stated in the study of the spacecraft attitude discussed in [61].

1.4 Overview of the thesis

This thesis has different parts to be analysed in order to have a complete study of a flexible spacecraft. Firstly, the robotic manipulator dynamics model has been studied and implemented in MATLAB/SIMULINK environment, and a PID controller has been chosen to achieve the desired joint angles. Subsequently, the attitude dynamics and kinematics of the spacecraft is studied and modelled. In addition, the flexible solar panels dynamics has been added to the model and the first results are obtained. A finite element analysis with PATRAN/NASTRAN was required in order to obtain the natural modes, frequencies, and eigenvectors useful for the model implementation. Once the dynamics model of the flexible spacecraft was completed, the attention was focused on the GNC system for a flexible spacecraft, in particular the choice of two attitude controllers, instead of a guidance and control strategy. A LQR and ADRC algorithms were implemented in MATLAB/SIMULINK with the goal of achieving the desired orientation, and maintaining the correct attitude even after the disturbances due to the robotic arm and the solar panels. A tuning of all the parameters of the two controllers was required to obtain a satisfactory performance. The work is completed with the realization of the spacecraft CAD in SolidWorks, and the use of the 3D World Editor tool for the animation of the solar panels' deployment, an attitude manoeuvre, and the movement of the robotic manipulator.

Now a general overview of the thesis is summarized as follows:

- Chapter 2: all the system mathematical models of this thesis are introduced and divided in three main sections: attitude kinematics and dynamics, space manipulator, and flexible spacecraft.
- Chapter 3: the control strategies are presented, both for the robotic manipulator and the attitude control. Firstly, the generic PID controller is discussed and then applied to a robotic arm. After that, the LQR with active disturbance rejection through the implementation of the ADRC algorithm is argued.
- Chapter 4: this is the part where the simulation scenario is reported, and all the results regarding the previous sections can be found.
- Chapter 5: the conclusions and future works are discussed.

Chapter 2

System mathematical model

The spacecraft model is constituted by three main parts: the main body satellite, a 2 Degree-Of-Freedom (DOF) robotic manipulator with two links and four flexible solar panels. In Fig. 2.1 the body frame $\mathcal{F}_B = (x_B, y_B, z_B)$ is fixed to the main body and it has the origin in its Center of Mass (CoM). The x axis is parallel to the longer edge of the spacecraft and it is in the direction of the deployed robotic arm, the z axis is parallel to the shorter edge of the spacecraft and the y axis completes the right-handed Cartesian triad. The body frame represents the orientation of the spacecraft with respect to an inertial reference frame. The robotic arm is a planar manipulator in the xz plane, while the solar panels are deployed in the y and z directions.

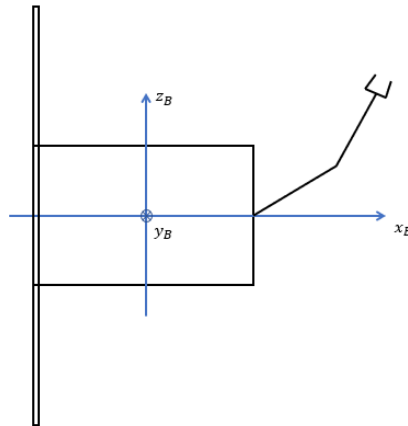


Figure 2.1: The scheme of flexible spacecraft with robotic arm and solar panels.

PRoximate Object Close flyby with Optical Navigation (PROCYON) has been chosen as the main body of the spacecraft (Fig. 2.2). It is an asteroid flyby space probe for deep space exploration, developed by the University of Tokyo (UT) and

Japan Aerospace Exploration Agency/Institute of Space and Astronautical Science (JAXA/ISAS). PROCYON was launched on the 3rd December, 2014 together with the Hayabusa2 asteroid landing probe. The mission had two main goals: the demonstration of a 50-kg class micro-spacecraft bus system for deep space exploration, and the close flyby of an asteroid, including the scientific observation mission ('geocorona' imaging mission) [62].

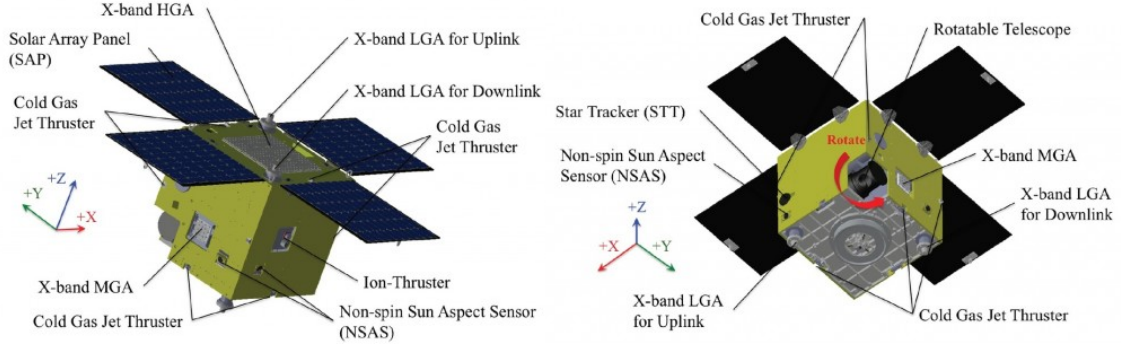


Figure 2.2: PROCYON top and bottom views (Image credits: JAXA/UT).

In the following sections the mathematical models of the attitude spacecraft, the manipulator and the flexible solar panels are discussed. A hybrid approach is used for implementing the main body attitude dynamics, including the solar panels, and the manipulator dynamics.

2.1 Attitude kinematics and dynamics

In this section a discussion about attitude dynamics and kinematics of a rigid body is done. The attitude kinematics of the spacecraft is studied through the quaternions, while Euler's equation is used for the attitude dynamics implementation. After that, a brief overview about internal and external torques acting on the spacecraft is done.

2.1.1 Attitude kinematics

The attitude kinematics of the spacecraft is described through Euler parameters, known as quaternions. A quaternion \mathbf{q} is a four-component vector composed by a three-vector part \mathbf{q}_v and scalar part q_0 :

$$\mathbf{q} = \begin{bmatrix} q_0 \\ \mathbf{q}_v \end{bmatrix} \quad (2.1)$$

where $\mathbf{q}_v = [q_1, q_2, q_3]^T$.

The kinematics equation for the quaternion is in the form [63]:

$$\dot{\mathbf{q}} = \frac{1}{2} \Xi(\mathbf{q}) \boldsymbol{\omega} \quad (2.2)$$

where $\Xi(\mathbf{q})$ is defined by:

$$\Xi(\mathbf{q}) = \begin{bmatrix} q_0 \mathbf{I}_3 + \mathbf{q}_v^x \\ -\mathbf{q}_v^T \end{bmatrix} \quad (2.3)$$

where $\mathbf{I}_3 \in \mathbb{R}^{3 \times 3}$ is the identity matrix and $\mathbf{q}_v^x \in \mathbb{R}^{3 \times 3}$ is the skew-symmetric matrix:

$$\mathbf{q}_v^x = \begin{bmatrix} 0 & -q_3 & q_2 \\ q_3 & 0 & -q_1 \\ -q_2 & q_1 & 0 \end{bmatrix} \quad (2.4)$$

2.1.2 Attitude dynamics

The main body is assumed to be a rigid body. The conservation of angular momentum is used to compute the equations for the attitude dynamics of a rigid body [63], known as *Euler's equation*:

$$\dot{\mathbf{H}}_I = \mathbf{M}_I \quad (2.5)$$

In particular, this equation tells that \mathbf{H}_I is constant in absence of any external torques. This equation can be written in a body reference frame, due to the easier expression of the external torques in this frame:

$$\dot{\mathbf{H}}_B = \mathbf{M}_B - \boldsymbol{\omega}_B^{BI} \times \mathbf{H}_B \quad (2.6)$$

where $\boldsymbol{\omega}_B^{BI}$ is the angular velocity of the spacecraft in the body frame. The angular momentum expressed in the body frame is given by:

$$\mathbf{H}_B = \mathbf{J}_B \boldsymbol{\omega}_B^{BI} \quad (2.7)$$

where \mathbf{J}_B is the moment of inertia expressed in the body frame. Combining (2.6) with (2.7), *Euler's rotational equation* is obtained:

$$\dot{\boldsymbol{\omega}}_B^{BI} = (\mathbf{J}_B)^{-1} [\mathbf{M}_B - \boldsymbol{\omega}_B^{BI} \times (\mathbf{J}_B \boldsymbol{\omega}_B^{BI})] \quad (2.8)$$

When a set of principal axes is chosen as the body axes, the inertia tensor \mathbf{J}_B is diagonal [64] :

$$\mathbf{J}_B = \begin{bmatrix} J_x & 0 & 0 \\ 0 & J_y & 0 \\ 0 & 0 & J_z \end{bmatrix} \quad (2.9)$$

The Euler's equation of motion for a rigid body are given by:

$$\begin{cases} J_x \dot{\omega}_1 + (J_z - J_y) \omega_2 \omega_3 = M_x \\ J_y \dot{\omega}_2 + (J_x - J_z) \omega_3 \omega_1 = M_y \\ J_z \dot{\omega}_3 + (J_y - J_x) \omega_1 \omega_2 = M_z \end{cases} \quad (2.10)$$

Eq.(2.8) and the quaternion kinematics equation (2.2) provide a complete description of the motion of a rigid body [63].

Internal torques

The spacecraft is constituted by several parts connected by joints and cannot be considered as a single rigid body. There are internal torques acting on the spacecraft, due to the presence of reaction wheels (RWs), control moment gyros (CMGs), the flexibility of some bodies of the spacecraft, or the slosh of liquid fluids. In this section the reaction wheels dynamics is discussed. Reaction wheels are known as *momentum exchange* devices, due to the capability of generate internal torques to the spacecraft without changing the overall angular momentum. In this case a system of four reaction wheels is considered, as in PROCYON spacecraft. The RWs system is modelled with a first order filter and a saturation block for each wheel in SIMULINK environment (Fig. 2.3). The reaction wheels are subjected to two limitations: a torque saturation, due to the maximum torque that the wheels can provide for electrical limitation, and a momentum saturation, due to a mechanical limitation. When the wheel reaches the maximum velocity, it is not able to further accelerate and "desaturation" with reaction control thrusters or magnetotorquers is needed.

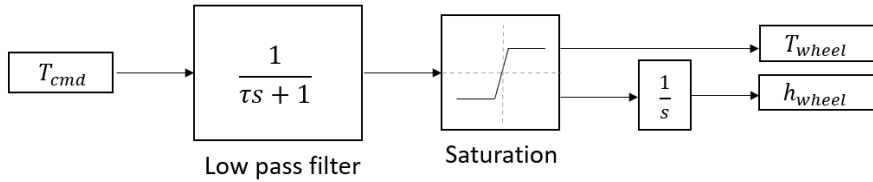


Figure 2.3: Reaction wheels model.

The reaction wheels block has the required control torque from the controller as

input, and gives the reaction wheels torque (2.11) and momentum (2.12) as output:

$$T_{wheel_i} = -\frac{1}{\tau_S + 1} \cdot T_{cmd_i} \quad (2.11)$$

$$h_{wheel_i} = \frac{1}{S} \cdot T_{wheel_i} \quad (2.12)$$

where $i = 1, \dots, n_a$, with n_a equal to the number of actuators. The four reaction wheels are set in a pyramidal configuration as in Fig. 2.4, where the wheels spin axis are pointing towards the faces of a pyramid with square base (Fig. 2.4).

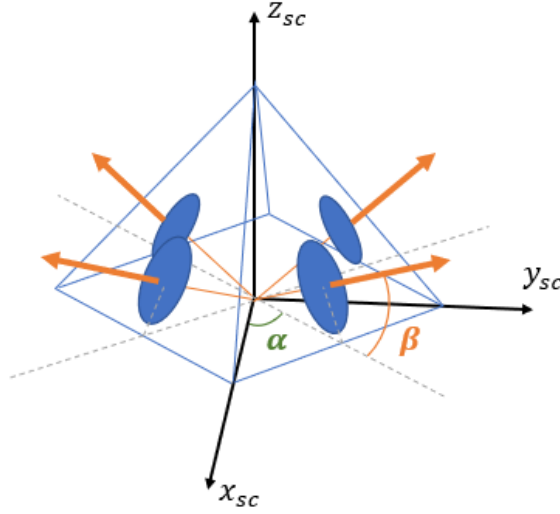


Figure 2.4: Reaction wheels pyramidal configuration.

The torque in Eq. (2.11), computed for each reaction wheel, has to be decomposed into the three inertia axis. For this purpose, a Z_{rws} (2.14) transformation matrix is used:

$$\begin{cases} h_x = h_1 \cos \beta \cos \alpha - h_2 \cos \beta \sin \alpha - h_3 \cos \beta \cos \alpha + h_4 \cos \beta \sin \alpha \\ h_y = h_1 \cos \beta \sin \alpha + h_2 \cos \beta \cos \alpha - h_3 \cos \beta \sin \alpha - h_4 \cos \beta \cos \alpha \\ h_z = h_1 \sin \beta + h_2 \sin \beta + h_3 \sin \beta + h_4 \sin \beta \end{cases} \quad (2.13)$$

$$\mathbf{Z}_{rws} = \begin{bmatrix} \cos \beta \cos \alpha & -\cos \beta \sin \alpha & -\cos \beta \cos \alpha & \cos \beta \sin \alpha \\ \cos \beta \sin \alpha & \cos \beta \cos \alpha & -\cos \beta \sin \alpha & -\cos \beta \cos \alpha \\ \sin \beta & \sin \beta & \sin \beta & \sin \beta \end{bmatrix} \quad (2.14)$$

The final expressions for the torque and angular momentum of the reaction wheels are given by:

$$\mathbf{M}_{rws} = \mathbf{Z}_{rws}^{3 \times n_a} \cdot \begin{bmatrix} T_{wheel_1} \\ \vdots \\ T_{wheel_{n_a}} \end{bmatrix} \quad (2.15)$$

$$\mathbf{H}_{rws} = \mathbf{Z}_{rws}^{3 \times n_a} \cdot \begin{bmatrix} h_{wheel_1} \\ \vdots \\ h_{wheel_{n_a}} \end{bmatrix} \quad (2.16)$$

The generalization of the Euler's equation (2.8), including the reaction wheels, is given by:

$$\dot{\boldsymbol{\omega}}_B^{BI} = (\mathbf{J}_B)^{-1} [\mathbf{M}_B - \mathbf{M}_B^{rws} - \boldsymbol{\omega}_B^{BI} \times (\mathbf{J}_B \boldsymbol{\omega}_B^{BI} + \mathbf{H}_B^{rws})] \quad (2.17)$$

where the angular momentum of the reaction wheels is given by:

$$\mathbf{H}_B^{rws} = \mathbf{J}_{rws} \boldsymbol{\omega}_{rws} \quad (2.18)$$

with \mathbf{J}_{rws} is the reaction wheels moment of inertia, and $\boldsymbol{\omega}_{rws}$ is the angular velocity. The negative sign before \mathbf{M}_B^{rws} on the right side reflects Newton's third law of motion.

External torques

External torques involve the interaction between the spacecraft and the entities external to it. In this thesis the spacecraft attitude dynamics is studied in a different way with respect to the robotic manipulator. Hence, the manipulator represents an external disturbance for the spacecraft, and it causes the change of the overall momentum of the spacecraft. In general a spacecraft is subjected to different perturbations in space, such as gravity gradient, magnetic field, aerodynamic torque, or solar radiation pressure torque, due to the space environment. In this case the only external disturbance of the robotic arm is considered, due to its higher value compared with the other disturbances.

Refer to the section (2.2) for the discussion about the robotic manipulator dynamics and the disturbance torques acting on the spacecraft. For the principle of action and reaction, the torques generated by the manipulator are considered with a negative sign in Euler's equation. Hence, Eq. (2.16) can be written as follows:

$$\dot{\boldsymbol{\omega}}_B^{BI} = (\mathbf{J}_B)^{-1} [\mathbf{M}_{ext} - \mathbf{M}_B^{rws} - \boldsymbol{\omega}_B^{BI} \times (\mathbf{J}_B \boldsymbol{\omega}_B^{BI} + \mathbf{H}_B^{rws})] \quad (2.19)$$

where \mathbf{M}_{ext} is the external disturbance due to the robotic arm.

2.1.3 State-space equation

Euler's equation (2.8) is expressed in a non-linear form. In this section the linearisation of the dynamics equation is reported in order to apply the LQR controller discussed in the following section. As reported in [59], the angular velocity of the spacecraft in body axes can be linearised as:

$$\boldsymbol{\omega}_B^{BI} = \begin{bmatrix} \dot{\phi} - \psi\omega_0 \\ \dot{\theta} - \omega_0 \\ \dot{\psi} + \phi\omega_0 \end{bmatrix} \quad (2.20)$$

where ω_0 is the initial orbital angular velocity of the spacecraft given by:

$$\omega_0 = \sqrt{\frac{\mu}{r^3}} \quad (2.21)$$

where $\mu = 3.98600411 \times 10^{14} \text{ m}^3/\text{s}^2$ is the gravitational parameter, and $r = R_{\oplus} + h$ is the sum of the Earth radius and the altitude. The time derivation is given by:

$$\dot{\boldsymbol{\omega}}_B^{BI} = \begin{bmatrix} \ddot{\phi} - \dot{\psi}\omega_0 \\ \ddot{\theta} \\ \ddot{\psi} + \dot{\phi}\omega_0 \end{bmatrix} \quad (2.22)$$

In these equations, Euler angles are roll ϕ , pitch θ and yaw ψ . ϕ represents the rotation about the x-axis, θ is the rotation about y-axis, and ψ is the rotation about z-axis. Substituting Eqs. (2.20) and (2.22) in Eq. (2.10), the following mathematical models are obtained:

$$\begin{cases} \ddot{\phi} = \frac{I_z - I_y}{I_x} \omega_0^2 \phi + \frac{I_x - I_y - I_z}{I_x} \omega_0 \dot{\psi} + \frac{\tau_x}{I_x} \\ \ddot{\theta} = \frac{\tau_y}{I_y} \\ \ddot{\psi} = -\frac{I_y - I_x}{I_z} \omega_0^2 \psi - \frac{I_z + I_x - I_y}{I_z} \omega_0 \dot{\phi} + \frac{\tau_z}{I_z} \end{cases} \quad (2.23)$$

where $\mathbf{M}_{RW} = [\tau_x, \tau_y, \tau_z]^T$ is the control torque given by the reaction wheels.

The state-space equation is in the form:

$$\dot{\mathbf{x}}(t) = \mathbf{A}\mathbf{x}(t) + \mathbf{B}\mathbf{u}(t) \quad (2.24)$$

where the states and matrices are defined as follow:

$$\mathbf{x} = \begin{bmatrix} \phi \\ \theta \\ \psi \\ \dot{\phi} \\ \dot{\theta} \\ \dot{\psi} \end{bmatrix}, \dot{\mathbf{x}} = \begin{bmatrix} \dot{\phi} \\ \dot{\theta} \\ \dot{\psi} \\ \ddot{\phi} \\ \ddot{\theta} \\ \ddot{\psi} \end{bmatrix} \quad (2.25)$$

$$\mathbf{u} = \begin{bmatrix} \tau_x \\ \tau_y \\ \tau_z \end{bmatrix} \quad (2.26)$$

$$\mathbf{A} = \begin{bmatrix} 0 & 0 & 0 & 1 & 0 & 0 \\ 0 & 0 & 0 & 0 & 1 & 0 \\ 0 & 0 & 0 & 0 & 0 & 1 \\ \frac{\omega_0^2(I_z - I_y)}{I_x} & 0 & 0 & 0 & 0 & \frac{\omega_0(I_x - I_y + I_z)}{I_x} \\ 0 & 0 & 0 & 0 & 0 & 0 \\ 0 & 0 & -\frac{\omega_0^2(I_y - I_x)}{I_z} & \frac{\omega_0(I_y - I_x - I_z)}{I_z} & 0 & 0 \end{bmatrix} \quad (2.27)$$

$$\mathbf{B} = \begin{bmatrix} 0 & 0 & 0 \\ 0 & 0 & 0 \\ 0 & 0 & 0 \\ \frac{1}{I_x} & 0 & 0 \\ 0 & \frac{1}{I_y} & 0 \\ 0 & 0 & \frac{1}{I_z} \end{bmatrix} \quad (2.28)$$

These equations can be written including the gravity-gradient term as an external disturbance, in the case of an Earth-pointing spacecraft. The gravity-gradient torque is given by [65]:

$$\begin{cases} T_{Gx} = 3\omega_0^2(J_z - J_y)\phi \\ T_{Gy} = 3\omega_0^2(J_z - J_x)\theta \\ T_{Gz} = 0 \end{cases} \quad (2.29)$$

The new matrix \mathbf{A} of the state-space equation, including the gravity-gradient term, is obtained:

$$\mathbf{A} = \begin{bmatrix} 0 & 0 & 0 & 1 & 0 & 0 \\ 0 & 0 & 0 & 0 & 1 & 0 \\ 0 & 0 & 0 & 0 & 0 & 1 \\ \frac{4\omega_0^2(I_z - I_y)}{I_x} & 0 & 0 & 0 & 0 & \frac{\omega_0(I_x - I_y + I_z)}{I_x} \\ 0 & \frac{3\omega_0^2(I_z - I_x)}{I_y} & 0 & 0 & 0 & 0 \\ 0 & 0 & \frac{\omega_0^2(I_x - I_y)}{I_z} & \frac{\omega_0(I_y - I_x - I_z)}{I_z} & 0 & 0 \end{bmatrix} \quad (2.30)$$

In this thesis Eq.(2.27) is used.

2.2 Space manipulator

In this section the robotic manipulator dynamics is presented. There are two approaches to model a manipulator dynamics:

- Newton-Euler formulation
- Lagrange Formulation

In this thesis the Lagrange Formulation is used, hence an energy-based approach is proposed in order to obtain the dynamic equations of motion in a closed form.

2.2.1 Lagrangian Equations

The *Lagrangian* of a mechanical system is composed by the difference between its *kinetic energy* \mathcal{T} and *potential energy* \mathcal{V} [66]:

$$\mathcal{L} = \mathcal{T} - \mathcal{V} \quad (2.31)$$

All the interactions that are not derived by a potential energy are considered as generalized Lagrangian forces.

The Lagrangian equation is given by the following expression:

$$\frac{d}{dt} \frac{\partial \mathcal{L}}{\partial \dot{q}_i} - \frac{\partial \mathcal{L}}{\partial q_i} = \mathcal{Q}_i, \quad i = 1, \dots, N \quad (2.32)$$

where:

- \mathcal{L} is a scalar function of (q, \dot{q}) ;
- $q_i, i = 1, \dots, N$ are the components of the generalized Lagrangian coordinates vector q ;

- $Q_i, i = 1, \dots, N$ are the generalized Lagrangian forces.

Substituting Eq.(2.31) in Eq. (2.32), the Lagrangian equation can be written as:

$$\frac{d}{dt} \frac{\partial \mathcal{T}}{\partial \dot{q}_i} - \frac{\partial \mathcal{T}}{\partial q_i} + \frac{\partial \mathcal{V}}{\partial q_i} = Q_i, \quad i = 1, \dots, N \quad (2.33)$$

2.2.2 Dynamics of the two-link planar manipulator

In this thesis a two-link planar manipulator with 2 DoF is considered, as shown in Fig. 2.5.

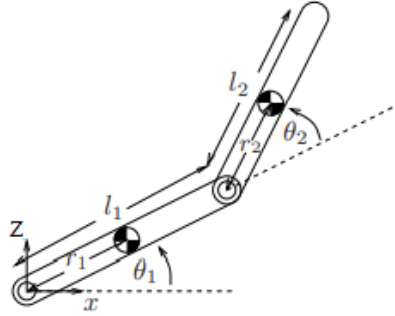


Figure 2.5: 2 DOF planar manipulator scheme [67].

To apply the Lagrange equation to the space manipulator, it is necessary to calculate the kinetic and potential energy of the links as a function of the joint angles and velocities [67]. Each of the two links is assumed to be a rigid body, hence the kinetic and potential energy can be defined in terms of its total mass and moments of inertia about each link's center of mass. The links are considered as homogeneous rectangular bars with mass m_i and moment of inertia tensor given by:

$$\mathbf{I}_i = \begin{bmatrix} I_{xi} & 0 & 0 \\ 0 & I_{yi} & 0 \\ 0 & 0 & I_{zi} \end{bmatrix}, \quad i = 1,2 \quad (2.34)$$

The inertia tensor is relative to a frame with its origin in the CoM of each link and aligned with the principle axes of the bar. In the scheme shown in Fig. 2.5, r_1 and r_2 are the distances between the i th-joint and the CoM of each link, l_1 and l_2 are the lengths of each link, and θ_1 and θ_2 are the joints angles.

A manipulator can have two types of joints: prismatic and revolute. Two revolute joints (Fig. 2.6) are considered in order to connect the main body of the spacecraft

and the first link, and the two links each other. Hence, each link as 1 DoF, represented by the θ_i joint angle, and a planar configuration is chosen.

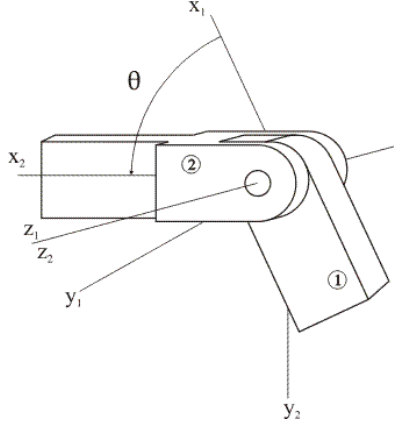


Figure 2.6: Revolute joint [68].

By returning to the Lagrange equation (2.33), in the case of a spacecraft the potential energy is assumed to be null due to the absence of gravity in space, and the rigidity of the links, without considering the flexibility. At this point, the kinematics of the mechanism is used in order to express the kinetic energy in terms of the generalized coordinates [67]. The manipulator reference frame shown in Fig. 2.5 is used to express the kinematics, and it has the origin in the first joint that connects the main body to the first link. The axes of this frame are parallel to the body frame presented in Fig. 2.2, with x-axis aligned with the two links when $\theta_1 = \theta_2 = 0$, and z-axis aligned with the first link when $\theta_1 = 90^\circ$.

From direct kinematics, the following expressions can be derived, based on the geometric method:

$$\begin{aligned}
 \bar{x}_1 &= r_1 c_1 & \dot{\bar{x}}_1 &= -r_1 s_1 \dot{\theta}_1 \\
 \bar{y}_1 &= r_1 s_1 & \dot{\bar{y}}_1 &= r_1 c_1 \dot{\theta}_1 \\
 \bar{x}_2 &= l_1 c_1 + r_2 c_{12} & \dot{\bar{x}}_2 &= -(l_1 s_1 + r_2 s_{12}) \dot{\theta}_1 - r_1 s_1 \dot{\theta}_1 \\
 \bar{y}_2 &= l_1 s_1 + r_2 s_{12} & \dot{\bar{y}}_2 &= (l_1 c_1 + r_2 c_{12}) \dot{\theta}_1 + r_2 c_{12} \dot{\theta}_2
 \end{aligned} \tag{2.35}$$

where $s_i = \sin \theta_i$, $s_{ij} = \sin(\theta_i + \theta_j)$, $c_i = \cos \theta_i$, and $s_{ij} = \cos(\theta_i + \theta_j)$.

Considering Eq.(2.31), the vector of the generalized coordinates is:

$$\mathbf{q} = \begin{bmatrix} \theta_1 \\ \theta_2 \end{bmatrix} \tag{2.36}$$

Letting the potential energy equal to zero, the Lagrange equation becomes:

$$\frac{d}{dt} \frac{\partial \mathcal{T}}{\partial \dot{q}_i} - \frac{\partial \mathcal{T}}{\partial q_i} = Q_i, \quad i = 1, 2 \quad (2.37)$$

The kinetic energy is given by:

$$\mathcal{T}(\theta, \dot{\theta}) = \frac{1}{2} m_1 \|\mathbf{v}_1\|^2 + \frac{1}{2} \boldsymbol{\omega}_1^T I_1 \boldsymbol{\omega}_1 + \frac{1}{2} m_2 \|\mathbf{v}_2\|^2 + \frac{1}{2} \boldsymbol{\omega}_2^T I_2 \boldsymbol{\omega}_2 \quad (2.38)$$

where:

$$\boldsymbol{\omega}_1 = \begin{bmatrix} 0 \\ \dot{\theta}_1 \\ 0 \end{bmatrix}, \quad \boldsymbol{\omega}_2 = \begin{bmatrix} 0 \\ \dot{\theta}_1 + \dot{\theta}_2 \\ 0 \end{bmatrix} \quad (2.39)$$

The motion of the manipulator is restricted to the xz plane, hence $\|\mathbf{v}_i\|$ is the magnitude of the xz velocity of the CoM and $\boldsymbol{\omega}_i$ is a vector in the direction of the y -axis, with $\|\boldsymbol{\omega}_1\| = \dot{\theta}_1$ and $\|\boldsymbol{\omega}_2\| = \dot{\theta}_1 + \dot{\theta}_2$.

The kinetic energy becomes:

$$\mathcal{T}(\theta, \dot{\theta}) = \frac{1}{2} m_1 (\dot{x}_1^2 + \dot{y}_1^2) + \frac{1}{2} I_{y1} \dot{\theta}_1^2 + \frac{1}{2} m_2 (\dot{x}_2^2 + \dot{y}_2^2) + \frac{1}{2} I_{y2} (\dot{\theta}_1^2 + \dot{\theta}_2^2) \quad (2.40)$$

where the moment of inertia are given by:

$$I_{y1} = \frac{1}{12} m_1 l_1^2, \quad I_{y2} = \frac{1}{12} m_2 l_2^2 \quad (2.41)$$

Substituting the Eqs. in (2.35) in (2.40), the following expression of the kinetic energy is obtained:

$$\mathcal{T}(\theta, \dot{\theta}) = \frac{1}{2} \begin{bmatrix} \dot{\theta}_1 \\ \dot{\theta}_2 \end{bmatrix}^T \begin{bmatrix} \alpha + 2\beta c_2 & \delta + \beta c_2 \\ \delta + \beta c_2 & \delta \end{bmatrix} \begin{bmatrix} \dot{\theta}_1 \\ \dot{\theta}_2 \end{bmatrix} \quad (2.42)$$

where

$$\begin{aligned} \alpha &= I_{y1} + I_{y2} + m_1 r_1^2 + m_2 (l_1^2 + r_2^2) \\ \beta &= m_2 l_1 r_2 \\ \delta &= I_{y2} + m_2 r_2^2 \end{aligned}$$

At this point, the partial derivatives of the kinetic energy with respect to q_i and \dot{q}_i , $\partial \mathcal{T} / \partial \dot{q}_i$ and $\partial \mathcal{T} / \partial q_i$, are computed and substituted into Lagrange's equations

(2.37). \mathcal{Q}_i represents the joint torques due to the actuators, $\boldsymbol{\tau} = [\tau_1, \tau_2]^T$. The final equations of motion obtained from the Lagrange formulation are in the form [69]:

$$\mathbf{M}(\mathbf{q})\ddot{\mathbf{q}} + \mathbf{C}(\mathbf{q}, \dot{\mathbf{q}})\dot{\mathbf{q}} = \boldsymbol{\tau} \quad (2.43)$$

where:

- \mathbf{M} is the non-linear symmetric mass matrix;
- \mathbf{C} contains the components associated with the centrifugal and Coriolis terms;
- $\boldsymbol{\tau}$ is the vector of generalized external forces.

After some calculation, the following equations of motion for the dynamics of a 2 DoF robotic manipulator are obtained:

$$\tau_1 = [(m_1 + m_2)l_1^2 + m_2l_2^2 + 2m_2l_1l_2c_2]\ddot{\theta}_1 + [m_2l_2^2 + m_2l_1l_2c_2]\ddot{\theta}_2 - 2m_2l_1l_2s_2\dot{\theta}_1\dot{\theta}_2 - m_2l_1l_2s_2\dot{\theta}_2^2 \quad (2.44)$$

$$\tau_2 = (m_2l_2^2 + m_2l_1l_2c_2)\ddot{\theta}_1 + m_2l_2^2\ddot{\theta}_2 + m_2l_1l_2s_2\dot{\theta}_1^2 \quad (2.45)$$

These dynamics equations can be resumed in the following form, as reported in [67]:

$$\begin{bmatrix} \alpha + 2\beta c_2 & \delta + \beta c_2 \\ \delta + \beta c_2 & \delta \end{bmatrix} \begin{bmatrix} \ddot{\theta}_1 \\ \ddot{\theta}_2 \end{bmatrix} + \begin{bmatrix} -\beta s_2 \dot{\theta}_2 & -\beta s_2(\dot{\theta}_1 + \dot{\theta}_2) \\ \beta s_2 \dot{\theta}_1 & 0 \end{bmatrix} \begin{bmatrix} \dot{\theta}_1 \\ \dot{\theta}_2 \end{bmatrix} = \begin{bmatrix} \tau_1 \\ \tau_2 \end{bmatrix} \quad (2.46)$$

2.3 Flexible Spacecraft

This thesis also deals with the problem of the spacecraft with flexible structures. The appendages of a spacecraft consist of lightweight, flexible, deployable solar panels, antennas, or booms [70] (Fig. 2.7). Flexible spacecraft is expected to achieve high pointing and fast attitude manoeuvring, that can introduce levels of vibration to flexible appendages due to the rigid-flexible coupling effect, which can cause the deterioration of its pointing performance [71]. The attitude controllers perform some functions such as pointing the antennas in a desired direction, pointing solar panels toward the sun, keeping sensors and equipment away from the sun's light and heat [70]. Attitude manoeuvres can create significant vibration in the satellite body. This section aims at modelling the dynamics of the solar panels and the coupling effect between the rigid and flexible parts.



Figure 2.7: Flexible spacecraft appendages [72].

2.3.1 Flexible Spacecraft Dynamics

The flexible part of the spacecraft is represented by the four solar panels of PROCYON spacecraft (Fig. 4.7).

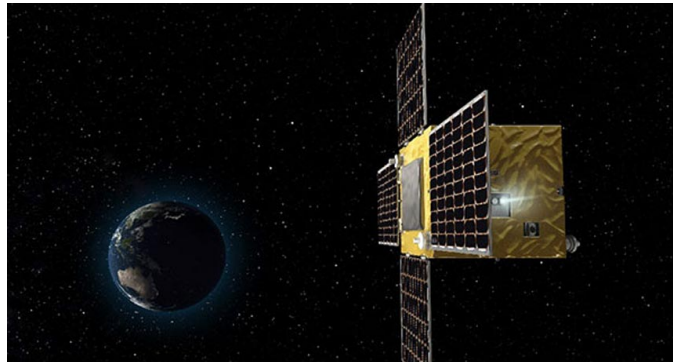


Figure 2.8: Solar panels of PROCYON spacecraft [73].

The Euler's equation (2.19) is written including the flexible appendages. The flexible dynamic equations are given by [74]:

$$\mathbf{J}\dot{\boldsymbol{\omega}} + \boldsymbol{\delta}^T \ddot{\boldsymbol{\eta}} = \mathbf{M}_{ext} + \mathbf{M}_{RW} - \boldsymbol{\omega} \times (\mathbf{J}\boldsymbol{\omega} + \mathbf{H}_{RW} + \boldsymbol{\delta}^T \dot{\boldsymbol{\eta}}) \quad (2.47)$$

$$\ddot{\boldsymbol{\eta}} + \mathbf{C}\dot{\boldsymbol{\eta}} + \mathbf{K}\boldsymbol{\eta} = -\boldsymbol{\delta}\dot{\boldsymbol{\omega}} \quad (2.48)$$

Eq. (2.47) represents the Euler's equation, including the flexible solar panels, in body reference frame. The rigid dynamics of the total angular momentum is given by [74]:

$$\boldsymbol{\chi} = \mathbf{J}\boldsymbol{\omega} + \boldsymbol{\delta}^T \dot{\boldsymbol{\eta}} \quad (2.49)$$

where:

- \mathbf{J} represents the symmetric inertia matrix of the whole structure, that is the sum of the main body's inertia matrix \mathbf{J}_{mb} , positive defined, and a symmetric inertia matrix due to the flexible structure;
- $\boldsymbol{\delta}$ is the coupling matrix between the elastic and rigid structures;
- $\boldsymbol{\eta}$ is the modal coordinate vector

Eq. (2.48) describes the flexible dynamics, under the assumption of small elastic deformations. \mathbf{K} and \mathbf{C} are defined as follow:

$$\mathbf{K} = \text{diag} \{ \omega_{ni}^2, i = 1, \dots, N \} \quad (2.50)$$

$$\mathbf{C} = \text{diag} \{ 2\zeta_i \omega_{ni}, i = 1, \dots, N \} \quad (2.51)$$

Eqs. (2.50) and (2.51) are respectively the stiffness matrix and the damping matrix. N is the number of elastic modes, ω_{ni} are the natural frequencies, and ζ_i are the corresponding damping ratios. In this work, the damping matrix is obtained from the stiffness matrix multiplied by a coefficient γ :

$$\mathbf{C} = \gamma \mathbf{K} \quad (2.52)$$

It is indeed not easy to compute the damping ratios without a detailed structural model or a experimental analysis, but this problem is not part of the thesis topics. It is worth noting that the solar panels are four, as in PROCYON spacecraft. Therefore, four contributions represented by $\boldsymbol{\delta}_i, i = 1, \dots, n_{SAP}$ have to be considered in Euler's equations, with $n_{SAP} = 4$, number of solar panels:

$$\mathbf{H}_{SAP} = \sum_{i=1}^{n_{SAP}} \boldsymbol{\delta}_i^T \dot{\boldsymbol{\eta}}_i \quad (2.53)$$

$$\mathbf{M}_{SAP} = \sum_{i=1}^{n_{SAP}} \delta_i^T \ddot{\boldsymbol{\eta}}_i \quad (2.54)$$

where \mathbf{H}_{SAP} represents the contribution of the flexible parts to the total angular momentum, while \mathbf{M}_{SAP} is the contribution to the total disturbance torque acting on the spacecraft. The flexibility of the solar panels included in the model is an internal disturbance with respect to the spacecraft, as in the case of the reaction wheels explained in section (2.1.2). Including Eqs. (2.53) and (2.54) in (2.47), the final expression of Euler's equation becomes:

$$\dot{\boldsymbol{\omega}} = \mathbf{J}^{-1}[-\boldsymbol{\omega} \times (\mathbf{J}\boldsymbol{\omega} + \mathbf{H}_{SAP} + \mathbf{H}_{RW}) - \mathbf{M}_{SAP} + \mathbf{M}_{ext} + \mathbf{M}_{RW}] \quad (2.55)$$

$$\ddot{\boldsymbol{\eta}}_i = -\delta_i \dot{\boldsymbol{\omega}} - (\mathbf{K}\boldsymbol{\eta}_i + \mathbf{C}\dot{\boldsymbol{\eta}}_i), \quad i = 1, \dots, n_{SAP} \quad (2.56)$$

It can be demonstrated that $\delta^T \delta$ represents the contribution of the flexible parts to the total inertia matrix [74]. Therefore, the total inertia matrix of the whole structure, that appears in Eq. (2.55), is defined as follow:

$$\mathbf{J} = \mathbf{J}_{mb} + \mathbf{J}_{SAP} \quad (2.57)$$

where:

$$\mathbf{J}_{SAP} = \sum_{i=1}^{n_{SAP}} \delta_i^T \delta_i \quad (2.58)$$

2.3.2 Coupling matrix

A particular attention is given to the interaction between spacecraft attitude control systems and flexible structures. The traditional assumption considers that the dynamic response to attitude control devices is uncoupled from vehicle vibrations, but some appendages cannot be designed with sufficient rigidity to justify it [75]. Therefore, it is necessary to compare the coupled equations of vibration with the attitude dynamics given by Euler's equation. This section is dedicated to the computation of the coupling matrix $\boldsymbol{\delta}$ between the flexible and rigid structures of the spacecraft, that appears in Eqs. (2.47) and (2.48). As reported in [76], the coupling matrix is defined as the following N by 3 matrix:

$$\bar{\boldsymbol{\delta}} = -\boldsymbol{\phi}^T \mathbf{M}(\boldsymbol{\Sigma}_{0E} - \boldsymbol{\Sigma}_{E0} \tilde{\mathbf{R}} - \tilde{\mathbf{r}} \boldsymbol{\Sigma}_{E0}) \quad (2.59)$$

where [75, 76]:

- $\boldsymbol{\delta}$ is the coupling matrix $6n \times 3$, with n equal to the number of sub-bodies in which each panel is divided. The bar over δ indicates that it is a truncated

matrix of dimensions $N \times 3$, with N equal to the number of appendages modal coordinates retained after truncation, or the normal modes;

- ϕ represents the matrix of the eigenvectors of the appendages of dimensions $6n \times 6n$. Also in this case, the bar over ϕ indicates the truncation of the eigenvectors matrix, defined as a $6n \times N$ matrix;
- \mathbf{M} is a $6n \times 6n$ matrix of masses and inertias of appendages sub-bodies;
- Σ_{0E} and Σ_{E0} are $6n \times 3$ matrix operators;
- \mathbf{R} is a 3×1 matrix, defined below. The (\sim) operator indicates the skew-symmetric 3×3 matrix.
- $\tilde{\mathbf{r}}$ is a $6n \times 6n$ matrix, defined below.

For simplicity, the bar over δ and ϕ truncated matrices is omitted. Now the matrices in all the matrices in Eq. (2.59) are defined. Before that, it is important to remember that n represents the total number of rigid bodies in a discrete parameter model of an appendage, as shown in Fig. 2.9.

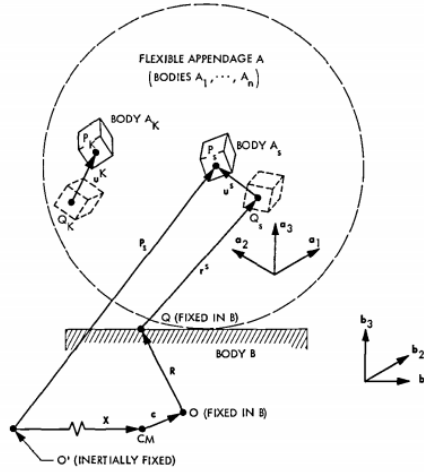


Figure 2.9: Discrete-parameter appendage sub-body coordinates [76].

In this work, it is assumed $n = 9$, hence each of the four solar panels has been divided into nine sub-panels, as shown in Fig. 2.10, where, for simplicity, the division of only one solar panel is represented.

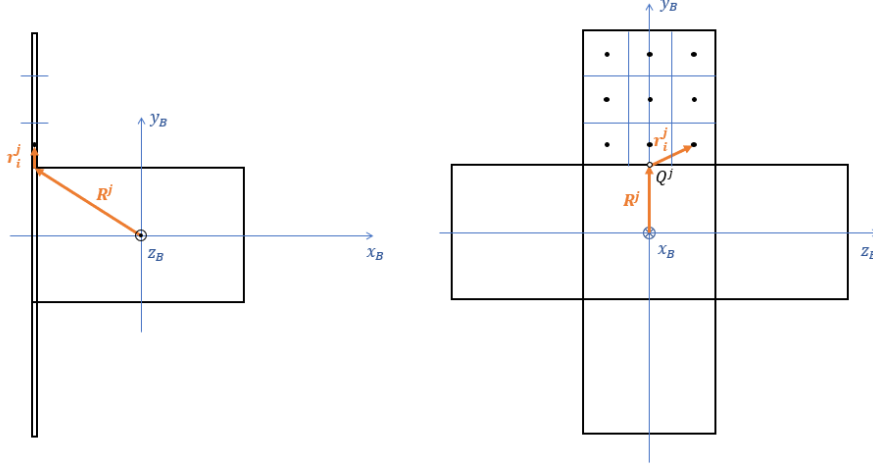


Figure 2.10: Front and upper view of spacecraft with sub-panels division.

The \mathbf{M} matrix is defined in terms of 3×3 partitioned matrices:

$$\mathbf{M} = \begin{bmatrix} \mathbf{m}^1 & 0 & 0 & 0 & \dots & 0 & 0 \\ 0 & \mathbf{I}^1 & 0 & 0 & \dots & 0 & 0 \\ 0 & 0 & \mathbf{m}^2 & 0 & \dots & 0 & 0 \\ 0 & 0 & 0 & \mathbf{I}^2 & \dots & 0 & 0 \\ \vdots & \vdots & \vdots & \vdots & \ddots & \vdots & \vdots \\ 0 & 0 & 0 & 0 & \dots & \mathbf{m}^n & 0 \\ 0 & 0 & 0 & 0 & \dots & 0 & \mathbf{I}^n \end{bmatrix} \quad (2.60)$$

For example, in the specific case of $n = 1$, the \mathbf{M} matrix becomes:

$$\mathbf{M}_1 = \begin{bmatrix} \mathbf{m}^i & 0 \\ 0 & \mathbf{I}^i \end{bmatrix} = \begin{bmatrix} m_1 & 0 & 0 & 0 & 0 & 0 \\ 0 & m_1 & 0 & 0 & 0 & 0 \\ 0 & 0 & m_1 & 0 & 0 & 0 \\ 0 & 0 & 0 & I_{x1} & 0 & 0 \\ 0 & 0 & 0 & 0 & I_{y1} & 0 \\ 0 & 0 & 0 & 0 & 0 & I_{z1} \end{bmatrix} \quad (2.61)$$

where $\mathbf{m}^i = m_i \mathbf{E}$, with \mathbf{E} equal to the identity matrix, and \mathbf{I}^i represents the sub-panel inertia tensor with respect to the sub-panel CoM. The \mathbf{M}^j matrix in the case of $n = 9$ sub-panels becomes:

$$\mathbf{M}^j = \begin{bmatrix} m_1 & 0 & 0 & 0 & 0 & 0 & \dots & 0 & 0 & 0 & 0 & 0 & 0 \\ 0 & m_1 & 0 & 0 & 0 & 0 & \dots & 0 & 0 & 0 & 0 & 0 & 0 \\ 0 & 0 & m_1 & 0 & 0 & 0 & \dots & 0 & 0 & 0 & 0 & 0 & 0 \\ 0 & 0 & 0 & I_{x1} & 0 & 0 & \dots & 0 & 0 & 0 & 0 & 0 & 0 \\ 0 & 0 & 0 & 0 & I_{y1} & 0 & \dots & 0 & 0 & 0 & 0 & 0 & 0 \\ 0 & 0 & 0 & 0 & 0 & I_{z1} & \dots & 0 & 0 & 0 & 0 & 0 & 0 \\ \vdots & \vdots & \vdots & \vdots & \vdots & \vdots & \ddots & \vdots & \vdots & \vdots & \vdots & \vdots & \vdots \\ 0 & 0 & 0 & 0 & 0 & 0 & \dots & m_n & 0 & 0 & 0 & 0 & 0 \\ 0 & 0 & 0 & 0 & 0 & 0 & \dots & 0 & m_n & 0 & 0 & 0 & 0 \\ 0 & 0 & 0 & 0 & 0 & 0 & \dots & 0 & 0 & m_n & 0 & 0 & 0 \\ 0 & 0 & 0 & 0 & 0 & 0 & \dots & 0 & 0 & 0 & I_{xn} & 0 & 0 \\ 0 & 0 & 0 & 0 & 0 & 0 & \dots & 0 & 0 & 0 & 0 & I_{yn} & 0 \\ 0 & 0 & 0 & 0 & 0 & 0 & \dots & 0 & 0 & 0 & 0 & 0 & I_{zn} \end{bmatrix} \quad (2.62)$$

where the index $j = 1, \dots, n_{SAP}$ represents the number of solar panels.

In general, Σ_{E0} and Σ_{0E} are defined as follow:

$$\Sigma_{E0} = \begin{bmatrix} \mathbf{E} \\ \mathbf{0} \\ \vdots \\ \mathbf{E} \\ \mathbf{0} \end{bmatrix}, \quad \Sigma_{0E} = \begin{bmatrix} \mathbf{0} \\ \mathbf{E} \\ \vdots \\ \mathbf{0} \\ \mathbf{E} \end{bmatrix} \quad (2.63)$$

where:

$$\mathbf{E} = \begin{bmatrix} 1 & 0 & 0 \\ 0 & 1 & 0 \\ 0 & 0 & 1 \end{bmatrix}, \quad \mathbf{0} = \begin{bmatrix} 0 & 0 & 0 \\ 0 & 0 & 0 \\ 0 & 0 & 0 \end{bmatrix} \quad (2.64)$$

For $n = 9$, Σ_{E0} and Σ_{0E} are composed by these 3×3 matrices repeated n times.

The term \mathbf{R} represents the vector from the CoM of the spacecraft to the j th-point Q^j , with $j = 1, \dots, n_{SAP}$. It is important to remember that in Eq.(2.59) all the matrices are expressed in the body-frame.

For $\mathbf{R} = [R_1, R_2, R_3]^T$, the term $\widetilde{\mathbf{R}}$ that appears in Eq.(2.59) is the corresponding skew-matrix:

$$\widetilde{\mathbf{R}} = \begin{bmatrix} 0 & -R_3 & R_2 \\ R_3 & 0 & -R_1 \\ -R_2 & R_1 & 0 \end{bmatrix} \quad (2.65)$$

For the computation of the matrix $\tilde{\mathbf{r}}$, the solar panels frames in Fig. 2.11 are considered. The \mathbf{r}_i^j vectors go from point Q^j , that represents the central joint between the main body and each solar panel, and the CoM of each sub-panel (2.10). It is worth noting that, after the computation of these vectors in each solar panel frame, they have to be transformed in the body reference frame.

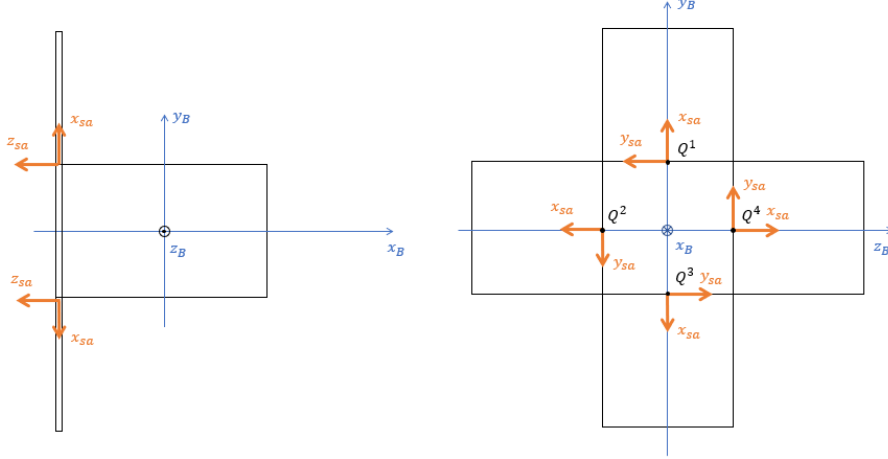


Figure 2.11: Solar panels reference frames.

In general the vector \mathbf{r} and the corresponding $\tilde{\mathbf{r}}$ that appears in Eq. (2.59) are defined as follow:

$$\mathbf{r} = \begin{bmatrix} \mathbf{r}_1 \\ 0 \\ \mathbf{r}_2 \\ 0 \\ \vdots \\ \mathbf{r}_n \\ 0 \end{bmatrix} \quad (2.66)$$

$$\tilde{\mathbf{r}} = \begin{bmatrix} \tilde{\mathbf{r}}_1 & 0 & 0 & 0 & \dots & 0 & 0 \\ 0 & 0 & 0 & 0 & \dots & 0 & 0 \\ 0 & 0 & \tilde{\mathbf{r}}_2 & 0 & \dots & 0 & 0 \\ 0 & 0 & 0 & 0 & \dots & 0 & 0 \\ \vdots & \vdots & \vdots & \vdots & \ddots & \vdots & \vdots \\ 0 & 0 & 0 & 0 & \dots & \tilde{\mathbf{r}}_n & 0 \\ 0 & 0 & 0 & 0 & \dots & 0 & 0 \end{bmatrix} \quad (2.67)$$

where each term $\tilde{\mathbf{r}}_i$, for $i = 1, \dots, n$, is the corresponding 3×3 skew-matrix.

Finally, the last term of Eq. (2.59) to be defined is the $6n \times 6n$ matrix of eigenvectors ϕ . In order to evaluate the eigenvectors for each solar panel, a Finite Element Method (FEM) analysis is done. For a complete explanation of this analysis, refer to the next section.

2.3.3 FEM analysis

A significant aspect of this thesis is the FEM analysis conducted with MSC Patran software and Nastran. This analysis is necessary in order to evaluate the natural modes and frequencies that appear in the stiffness and damping matrices (Eqs.(2.50) and (2.51)), and the eigenvectors. The geometry is realized in Patran (Fig. 2.12), with a central surface that represents the top part of the satellite, and the four surfaces for the solar panels. The panels are modelled as aluminium plates with the 2D shell property. The body is assumed to be rigid, and the four surfaces are connected to it through a fixed constraint. In Fig. 2.12, it can be noted a mesh with quad-elements. In order to obtain the values mentioned before, a modal analysis is done using the solver Nastran, and the post-processor Patran for the results.

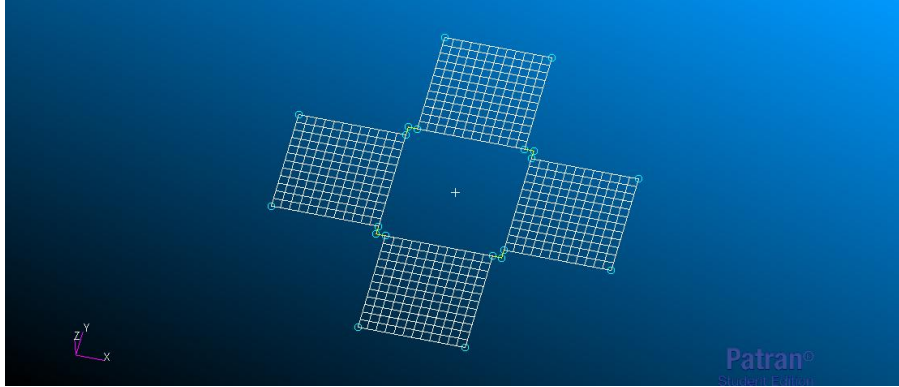


Figure 2.12: Solar panels model on Patran.

From these analysis, it is expected to obtain the shape modes in Fig. 2.13 for each solar panel, in the case of a fixed joint.

For the computation of the natural frequencies of the model, the approximate Raleigh-Ritz Method reported in [78] can also be used. According to this method, the natural frequencies in $[rad/s]$ of a cantilever plate of dimensions $a \times b \times h$ can be expressed by:

$$\omega_n = \frac{\lambda_n}{a^2} \sqrt{\frac{D}{\rho n}} \quad (2.68)$$

where $D = Eh^3/[12(1 - \nu^2)]$ is the flexural rigidity of the plate, E is the Young's Modulus, ν is the Poisson's ratio, and ρ is the mass density. Known the aspect

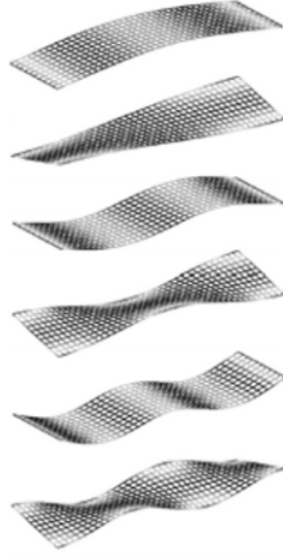


Figure 2.13: First six modes of a solar panel fixed to a satellite [77].

ratio (b/a), the value of the frequency parameter λ can be obtained, and from it the natural frequencies.

Finally, a discussion about the eigenvectors matrix ϕ can be done. As explained in section (2.3.1), the damping matrix is chosen after knowing the stiffness matrix, hence the FEM analysis is done without including the damping coefficient. In general, the free vibration of motion for a linear and undamped structure may be expressed in the matrix notation [78]:

$$\mathbf{M}\ddot{\mathbf{u}} + \mathbf{K}\mathbf{u} = \mathbf{0} \quad (2.69)$$

where \mathbf{M} is the mass matrix, \mathbf{K} is the stiffness matrix, \mathbf{u} is the displacement vector.

For a linear system, free vibrations are harmonic, and can be expressed in the form:

$$\mathbf{u} = \phi \sin \omega t \quad (2.70)$$

where ϕ is the eigenvector or mode shape, and ω is the natural frequency. Substituting this equation in Eq.(2.69), and after simplifying, the equation becomes:

$$(\mathbf{K} - \omega_i^2 \mathbf{M})\phi = 0 \quad (2.71)$$

that is also known as the eigenvalues problem.

In general, when a linear elastic structure is vibrating in free or forced vibration, its deflected shape at any given time is a linear combination of all of its normal modes [79]

$$\mathbf{u} = \sum_i \phi_i \xi_i \quad (2.72)$$

where \mathbf{u} is the vector of physical displacements, ϕ_i is the i -th mode shape, and ξ_i is the modal displacement.

Through the FEM analysis software, it is possible to obtain the eigenvectors for this model. The eigenvector matrix ϕ can be defined as follow:

$$\phi_n^N = \begin{bmatrix} \phi_1^1 & \phi_2^1 & \dots & \phi_n^1 \\ \phi_1^2 & \phi_2^2 & \dots & \phi_n^2 \\ \vdots & \vdots & \ddots & \vdots \\ \phi_1^N & \phi_2^N & \dots & \phi_n^N \end{bmatrix} \quad (2.73)$$

where n is the number of sub-panels each panel is divided in, and N is the number of shape modes. For the definition of the eigenvectors matrix, the eigenvectors of the nodes corresponding to the CoM of each sub-panels are considered. For each node and for a $N - th$ shape mode, a ϕ_i matrix, for $i = 1, \dots, n$, is defined:

$$\phi_i = [T_1, T_2, T_3, R_1, R_2, R_3] \quad (2.74)$$

where T_1, T_2, T_3 are the translational eigenvectors, and R_1, R_2, R_3 are the rotational eigenvectors obtained by the modal analysis with Patran/Nastran (Fig. (2.14)).

NATURAL FREQUENCY ANALYSIS			REAL EIGENVALUES				GENERALIZED	
NODE NO.	EXTRACTION ORDER	EIGENVALUE λ_i	RADIANS ω_i	CYCLES $\omega_i / 2\pi$	MASS	STIFFNESS		
1	1	9.000000E+00	3.000000E+00	4.774648E-01	1.000000E+00	9.000000E+00		
2	2	2.700000E+01	5.196152E+00	8.269933E-01	1.000000E+00	2.700000E+01		
EIGENVALUE = 9.000000E+00 CYCLES = 4.774648E-01			REAL EIGENVECTOR NO. 1					
POINT ID.	TYPE	T1	T2	T3	R1	R2	R3	
50	G	0.0	0.0	0.0	0.0	0.0	0.0	
51	G	5.000000E-01	0.0	0.0	0.0	0.0	0.0	
52	G	5.000000E-01	0.0	0.0	0.0	0.0	0.0	
53	G	0.0	0.0	0.0	0.0	0.0	0.0	
EIGENVALUE = 2.700000E+01 CYCLES = 8.269933E-01			REAL EIGENVECTOR NO. 2					
POINT ID.	TYPE	T1	T2	T3	R1	R2	R3	
50	G	0.0	0.0	0.0	0.0	0.0	0.0	
51	G	-5.000000E-01	0.0	0.0	0.0	0.0	0.0	
52	G	5.000000E-01	0.0	0.0	0.0	0.0	0.0	
53	G	0.0	0.0	0.0	0.0	0.0	0.0	

Figure 2.14: Real eigenvectors/eigenvalues from natural frequency analysis [79].

Chapter 3

Controllers

In this thesis different control strategies are analysed. In the case of the robotic manipulator, a simple Proportional-Integral-Derivative (PID) controller is adopted, in order to reach the desired angular position, while an Active Disturbance Rejection Control (ADRC) with a Linear Quadratic Regulator (LQR) as control law is implemented for the spacecraft attitude. In the following sections, a general discussion about these controllers is presented.

3.1 PID Controller

The first controller to be introduced is the PID controller. PID controllers are the most employed controllers in industrial field due to their capability to provide a satisfactory performance for many control problems [80]. The logic of the PID controller lies in the propagation of a weighted sum of the input signal, its integral, and its first derivative to the output [81]. The output signal in the time domain is given by:

$$y(t) = k_P \cdot x(t) + k_I \cdot \int x(t)dt + k_D \cdot \frac{dx(t)}{dt} \quad (3.1)$$

The input to the PID controller is the control error $\varepsilon(t)$, given by the difference between the reference signal and the actual signal measured by the sensors, as shown in Fig. 3.1. In the Laplace domain the transfer function is given by:

$$\frac{Y(s)}{X(s)} = k_P + \frac{k_I}{s} + k_D s = \frac{k_D s^2 + k_P s + k_I}{s} \quad (3.2)$$

The constants k_P, k_I and k_D are adjustable and optimized for the specific type of process and control goal.

Proportional component

A high proportional term k_P can lead to a low sensibility, small steady-state error,

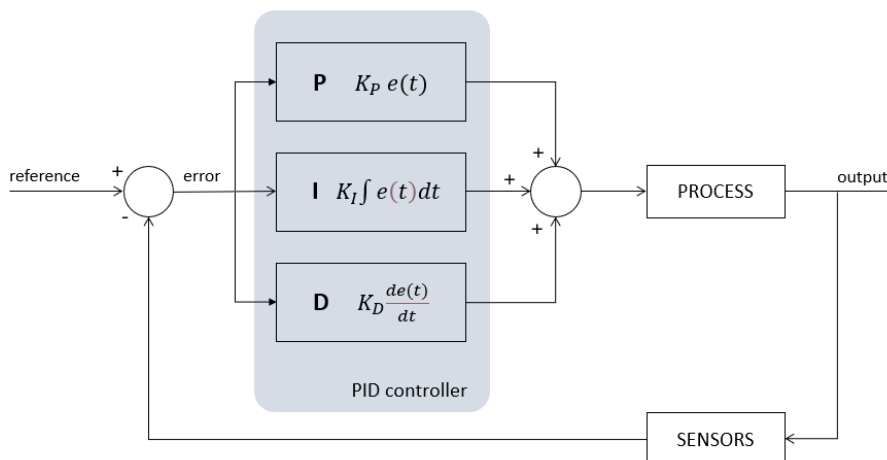


Figure 3.1: Block diagram of a PID controller.

and good disturbance rejection. On the other hand, k_P has some upper limits, either physical or related to stability and overshoot.

Integral component

The integral component k_I is responsible for eliminating the steady-state error. Indeed, if the input of the PID controller is the control error ε , then the integrator component changes the corrective action until $\varepsilon = 0$. Compared to k_P , the integral component is kept relatively small, due to undesirable transient responses, overshoot increase, and even instability.

Derivative component

The derivative component k_D helps providing a rapid transient response. If a transient disturbance or a sudden change of the set-point occur, then the first derivative is huge, and causes a correspondingly strong control action [81]. The derivative component also contributes to the increase of the system's stability.

Tab. 3.1 resumes the consequences of the increase of each PID gain [82]

Table 3.1: PID gains

	Rise Time	Overshoot	Settling Time	Steady State Error	Stability
$k_P \uparrow$	decrease	increase	small increase	decrease	degrade
$k_I \uparrow$	small decrease	increase	increase	large decrease	degrade
$k_D \uparrow$	small decrease	decrease	decrease	minor change	improve

3.1.1 Robotic arm control

The PID controller is applied to the two links robotic manipulator. A different PID controller is considered for each link in order to control separately the two parts of the robotic manipulator. The input of the PID controller is given by the angular position error, defined as the difference between the desired joint angle and the actual joint angle output from the plant, as shown in Fig. 3.2.

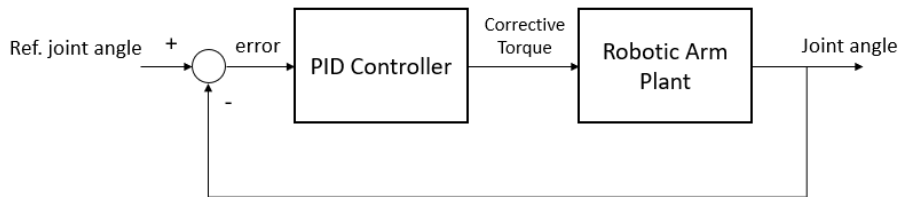


Figure 3.2: Block diagram of the robotic manipulator PID controller

The PID controller returns the corrective actuator's torque that has given as input to the corresponding link, in order to achieve the desired joint angle.

3.2 Attitude control

In this section the attitude control strategy is presented. As told in the previous sections, a Active Disturbance Rejection Control, together with a Linear Quadratic Regulator, is implemented to cancel all the disturbances acting on the model and achieve the desired attitude. Firstly, the traditional ADRC is described, and then the combination of ADRC and LQR is presented.

3.2.1 ADRC

Active disturbance rejection control (Fig. 3.3) technology was proposed in 1998 by Jingqing Han, and first introduced in English by Z. Gao [83]. The main idea of this new control strategy is to estimate and compensate the unknown internal and external disturbances as one signal by using an Extended State Observer (ESO), and then to impart this signal to the control law. ADRC consists of a Tracking Differentiator (TD), an Extended State Observer and an error-based control law. It has fine control performances, such as quick response, small overshoot and good robustness because of its non-linear dynamic structure. For these reasons, it easily finds application in aviation, aerospace, power and chemical industries [84]. The ADRC main parts can be resumed as follows [84, 85]:

- The Tracking Differentiator is used to arrange the transition process for the input of a system in order to achieve smooth input signals and differential ones.
- The Extended State Observer compensates internal and external disturbances.
- The non linear equation error feedback controller combines the tracking signal and differential signal from TD, and the system's estimated states given by ESO to achieve the control signal.

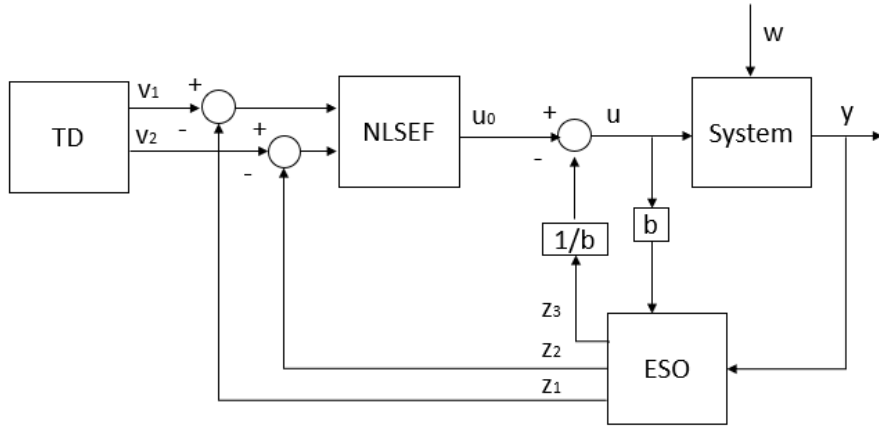


Figure 3.3: Traditional ADRC configuration

In this thesis an ADRC controller is developed, including TD, ESO and an LQR as control law. The Linear Quadratic Regulator is chosen, instead of the classic non linear controller proposed by Han, in order to achieve an optimal behaviour response from the system [83].

Tracking Differentiator

The Tracking Differentiator algorithm is based on differential signals. These signals play a significant role in control practices, but they are suggested to noise corruption. Firstly proposed by Han [86], the discrete-time optimal control based TD, with the noise-tolerant characteristic, is used in filtering and differentiation acquisition [87].

To construct a TD, the first procedure is to determine a control algorithm for a double-integral system, that is described by the following system:

$$\begin{cases} \dot{\mathbf{x}}_1 = \mathbf{x}_2, \\ \dot{\mathbf{x}}_2 = \mathbf{u}, \quad |\mathbf{u}| \leq r, \end{cases} \quad (3.3)$$

where r is a constant constraint of the control input. The resulting control algorithm that drives the state from any initial point to the origin in the shortest time is:

$$\mathbf{u} = -r \operatorname{sign} \left(\mathbf{x}_1 - \mathbf{v} + \frac{\mathbf{x}_2 |\mathbf{x}_2|}{2r} \right) \quad (3.4)$$

where \mathbf{v} is the desired value for \mathbf{x}_1 . The desired trajectory and its derivative are obtained solving the following equations [86]:

$$\begin{cases} \dot{\mathbf{v}}_1 = \mathbf{v}_2, \\ \dot{\mathbf{v}}_2 = -r \operatorname{sign} \left(\mathbf{v}_1 - \mathbf{v} + \frac{\mathbf{v}_2 |\mathbf{v}_2|}{2r} \right) \end{cases} \quad (3.5)$$

Extended State Observer

The most important part of the ADRC is the Extended State Observer [88]. ESO represents an augmented state with the role of estimating the states of the system, recognizing and eliminating all the internal and external disturbances.

For the sake of simplicity and clarity, a general Single Input Single Output (SISO) second-order system is taken as example [86], although this type of control algorithm is applicable to most non-linear Multi Input Multi Output (MIMO) systems, as in the case of this thesis. The SISO system is given by:

$$\begin{cases} \dot{\mathbf{x}}_1 = \mathbf{x}_2 \\ \dot{\mathbf{x}}_2 = f(\mathbf{x}_1, \mathbf{x}_2, \mathbf{w}(t), t) + b\mathbf{u} \\ \mathbf{y} = \mathbf{x}_1 \end{cases} \quad (3.6)$$

where \mathbf{y} is the output of the plant, measured and to be controlled, \mathbf{u} is the input, b is a constant, and $f(\mathbf{x}_1, \mathbf{x}_2, \mathbf{w}(t), t)$ is a multi-variable function of the states \mathbf{x}_1 and \mathbf{x}_2 , the external disturbances \mathbf{w} , and time t .

The objective is to make \mathbf{y} behave as desired using \mathbf{u} as the manipulative variable. For this purpose, $F(t) = f(\mathbf{x}_1(t), \mathbf{x}_2(t), \mathbf{w}(t), t)$ does not need to be expressively known, and is denoted as the "total disturbance".

Treating $F(t)$ as an additional state variable, $\mathbf{x}_3 = F(t)$, and letting $\dot{F}(t) = G(t)$, with $G(t)$ unknown, the original system (3.6) becomes:

$$\begin{cases} \dot{\mathbf{x}}_1 = \mathbf{x}_2 \\ \dot{\mathbf{x}}_2 = \mathbf{x}_3 + b\mathbf{u} \\ \dot{\mathbf{x}}_3 = G(t) \\ \mathbf{y} = \mathbf{x}_1 \end{cases} \quad (3.7)$$

The extended state observer is defined in the following form:

$$\begin{cases} \mathbf{e} = \mathbf{z}_1 - \mathbf{y} \\ \dot{\mathbf{z}}_1 = \mathbf{z}_2 - \beta_{01}\mathbf{e} \\ \dot{\mathbf{z}}_2 = \mathbf{z}_3 + b\mathbf{u} - \beta_{02}fal(\mathbf{e}, a_1, h) \\ \dot{\mathbf{z}}_3 = -\beta_{03}fal(\mathbf{e}, a_2, h) \end{cases} \quad (3.8)$$

where β_{01}, β_{02} , and β_{03} are the observer gains to be selected for the problem, a_1 and a_2 are assumed to be respectively equal to 0.5 and 0.25, h is the sampling period and $fal(\bullet)$ is the saturation non linear function [89] described as follow:

$$fal(\mathbf{e}, a, h) = \begin{cases} \frac{\mathbf{e}}{h^{1-a}}, & |\mathbf{e}| \leq h, \\ |\mathbf{e}|^a sign(\mathbf{e}), & |\mathbf{e}| > h \end{cases} \quad (3.9)$$

The output variable of ESO can track the state variable of the system, namely:

$$\mathbf{z}_1 \rightarrow \mathbf{x}_1, \mathbf{z}_2 \rightarrow \mathbf{x}_2, \mathbf{z}_3 \rightarrow \mathbf{x}_3$$

The inputs to ESO are the plant output \mathbf{y} and the control signal \mathbf{u} , while the output of the ESO provides the estimation of the states and the total disturbance.(fig. 3.4).

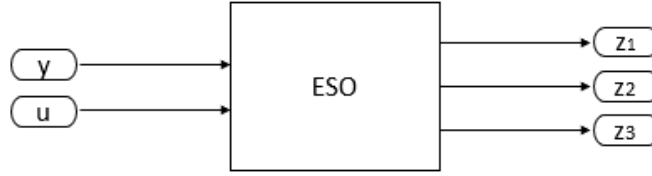


Figure 3.4: ESO input and output

The control signal of the system is given by:

$$\mathbf{u} = \mathbf{u}_0 - \frac{\mathbf{z}_3}{b_0} \quad (3.10)$$

where b_0 is a rough approximation of the coefficient b in the plant within a $\pm 50\%$ range [86], and \mathbf{u}_0 is the output of the controller. The system in the final form is given by:

$$\begin{cases} \dot{\mathbf{x}}_1 = \mathbf{x}_2 \\ \dot{\mathbf{x}}_2 = \mathbf{x}_3 + b_0 \left(\mathbf{u}_0 - \frac{\mathbf{z}_3}{b_0} \right) \\ \mathbf{y} = \mathbf{x}_1 \end{cases} \quad (3.11)$$

LQR control law

The LQR controller is designed to achieve a optimal behaviour, specifically, a fast response, a small overshoot, and no steady-state error [83]. The main idea of this controller is to find a cost function and minimize it [59]. After the cost function is minimized, the system states are fed back by a gain-matrix.

This is an optimization problem that consists of finding a linear control law of the following type:

$$\mathbf{u}(t) = -\mathbf{K}\mathbf{x}(t) \quad (3.12)$$

where \mathbf{K} is the feedback gain-matrix. The control signal \mathbf{u} has to be found in order to minimize the cost function. For this purpose, the Performance Index (PI) is defined:

$$J(\mathbf{x}, \mathbf{u}) = \frac{1}{2} \int_0^{\infty} (\mathbf{x}^T \mathbf{Q} \mathbf{x} + \mathbf{u}^T \mathbf{R} \mathbf{u}) dt \quad (3.13)$$

Substituting Eq.(3.12) in (3.13), the cost function in the following form is obtained:

$$J = \frac{1}{2} \int_0^{\infty} \mathbf{x}^T (\mathbf{Q} + \mathbf{K}^T \mathbf{R} \mathbf{K}) dt \quad (3.14)$$

where the feedback gain matrix \mathbf{K} is given by:

$$\mathbf{K} = \mathbf{R}^{-1} \mathbf{B}^T \mathbf{P} \quad (3.15)$$

where \mathbf{P} is the solution of algebraic *Riccati equation*:

$$\mathbf{A}^T \mathbf{P} + \mathbf{P} \mathbf{A} + \mathbf{Q} - \mathbf{P} \mathbf{B} \mathbf{R}^{-1} \mathbf{B}^T \mathbf{P} = 0 \quad (3.16)$$

In this equation $\mathbf{Q} \geq 0$, $\mathbf{R} > 0$, $\mathbf{P} \geq 0$ are symmetric, positive definite and semi-positive matrices, respectively defined as state and control weighting matrices:

$$\mathbf{Q} = \text{diag} [Q_1, Q_2, \dots, Q_{n_s}] \quad (3.17)$$

$$\mathbf{R} = \text{diag} [R_1, R_2, \dots, R_{n_a}] \quad (3.18)$$

In this case, n_s is the number of the states and n_a is the number of actuators.

\mathbf{Q} and \mathbf{R} matrices are adjusted in the developed MATLAB code until the desired performance is achieved. After that, the feedback gain matrix \mathbf{K} is calculated

in MATLAB using the following syntax command:

$$[\mathbf{K}, \mathbf{P}, \mathbf{E}] = \text{lqr}(\mathbf{A}, \mathbf{B}, \mathbf{Q}, \mathbf{R})$$

The state-feedback law in Eq.(3.12) minimizes the quadratic cost function for the state-space model. The MATLAB syntax *lqr* also returns the solution \mathbf{P} of the *Riccatiequation*, and the closed-loop eigenvalues $\mathbf{E} = \text{eig}(\mathbf{A} - \mathbf{B} * \mathbf{K})$. The block diagram of LQR optimal controller is shown in Fig. 3.5.

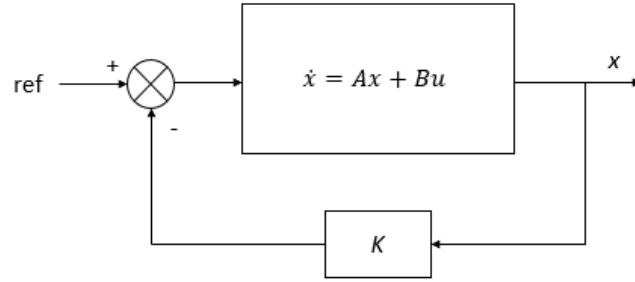


Figure 3.5: Block diagram of LQR optimal controller

3.2.2 ADRC/LQR for attitude control

In this section the ADRC/LQR controller is discussed for the specific case of the control attitude of a flexible spacecraft. The scheme in Fig. 3.6 illustrates the configuration of the ADRC/LQR used in this thesis.

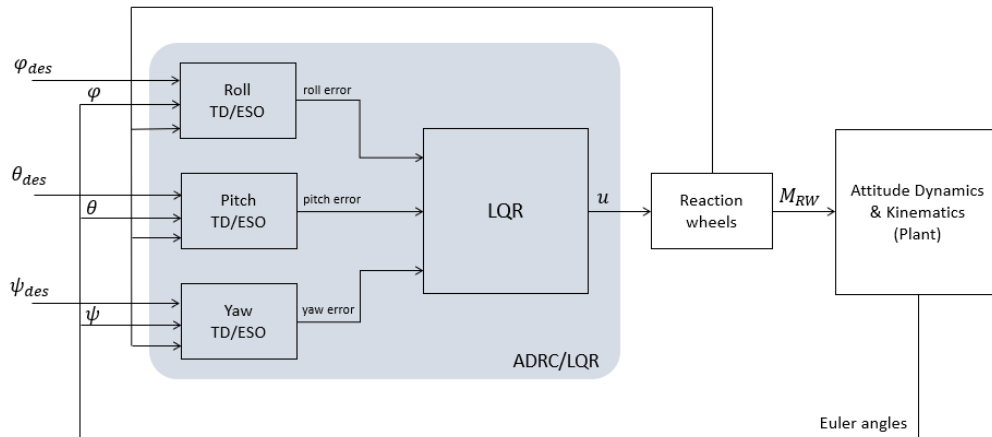


Figure 3.6: Block diagram of ADRC/LQR for attitude control

It is worth noting that three different TD and ESO systems have been considered for each Euler's angle, in order to control separately the roll, pitch, and yaw responses. The angle errors, derived from the TD/ESO system, are the input of the LQR controller, that is the same for each angle. Using the state-space model described in Chapter 2, the gain-matrix \mathbf{K} is found for the optimized problem. As can be seen from the scheme, the ESO only needs the informations from the plant and the reaction wheels block to estimate the total disturbance acting on the system.

The Euler equations for the flexible spacecraft, obtained in Chapter 2, are reported below:

$$\begin{cases} \dot{\boldsymbol{\omega}} = \mathbf{J}^{-1} \left[-\boldsymbol{\omega} \left(\mathbf{J}\boldsymbol{\omega} + \mathbf{H}_{RW} + \boldsymbol{\delta}^T \dot{\boldsymbol{\eta}} \right) + \mathbf{M}_{ext} + \mathbf{M}_{RW} - \boldsymbol{\delta}^T \ddot{\boldsymbol{\eta}} \right] \\ \ddot{\boldsymbol{\eta}} = -\boldsymbol{\delta} \dot{\boldsymbol{\omega}} - (\mathbf{K}\boldsymbol{\eta} + \mathbf{C}\dot{\boldsymbol{\eta}}) \end{cases} \quad (3.19)$$

In order to define the total disturbance, Eq.(3.19) can be written in the following form:

$$\dot{\mathbf{x}} = \mathbf{f} + \mathbf{b}\mathbf{u} \quad (3.20)$$

where

$$\mathbf{x} = \boldsymbol{\omega}, \quad \dot{\mathbf{x}} = \dot{\boldsymbol{\omega}} \quad (3.21)$$

$$\mathbf{b} = \mathbf{J}^{-1} \quad (3.22)$$

$$\mathbf{u} = \mathbf{M}_{RW} \quad (3.23)$$

The total disturbance acting on the system can be expressed as:

$$\mathbf{f} = \mathbf{J}^{-1} \left[-\boldsymbol{\omega} \left(\mathbf{J}\boldsymbol{\omega} + \mathbf{H}_{RW} + \boldsymbol{\delta}^T \dot{\boldsymbol{\eta}} \right) + \mathbf{M}_{ext} - \boldsymbol{\delta}^T \ddot{\boldsymbol{\eta}} \right] \quad (3.24)$$

In the specific case, three ESO system derive for the MIMO system considered. Hence, in Eq.(3.8) \mathbf{z}_1 represents the Euler angle, \mathbf{z}_2 its derivative, and \mathbf{z}_3 the disturbance acting in the corresponding axis. In this thesis the attention is particularly focused on the pitch axis, due to the higher disturbance given by the robotic manipulator.

Chapter 4

Simulation results

4.1 Overview of the mission

The mission scenario is characterized by a spacecraft orbiting in the LEO region for in-orbit servicing, including the capture of space debris, thanks to the robotic manipulator located on the bottom of the spacecraft. The spacecraft main body is the JAXA PROCYON micro-satellite, that includes the four solar panels and the system of four reaction wheels in a pyramidal configuration. The robotic arm configuration is chosen after a comparison of some space manipulators, as in [90]. In Tab. 4.1 the mission specifications and the main characteristics of the spacecraft, including the specification of PROCYON mission [62, 91, 92] used for this thesis, are resumed. Moreover, in Tab. 4.2 the actuators specifications for the robotic arm and reaction wheels are reported.

The next sections are organised as follows: an overview of the simulation environment is presented, referring to the main subsystems. After that, the results of this work are resumed in three main areas that have characterized this thesis: the robotic manipulator dynamics and control, the solar panel's FEM analysis and dynamics, and finally the attitude dynamics and control. Firstly, the manipulator and solar panels results are discussed in the case of the spacecraft being in the desired attitude. Subsequently, in the last section, the attitude dynamics and control is performed, and the influence of all the spacecraft subsystems is analysed.

Table 4.1: Mission specifications

	Specifications
Orbital parameters	Orbit altitude (LEO): 400 km Orbit angular velocity: 0.0011 <i>rad/s</i>
Spacecraft main body	Size: 0.55 m x 0.55 m x 0.67 m Mass: 67 Kg (including SAP) Moments of inertia in body frame: $I_x = 12.5102 \text{ Kg/m}^2$, $I_y = 15.5375 \text{ Kg/m}^2$, $I_z = 15.5375 \text{ Kg/m}^2$
Robotic arm	Size Link 1: 0.5 m Size Link 2: 0.5 m Mass Link 2: 3 Kg Mass Link 2: 3 Kg
Solar Array Panels (SAP)	Size of each SAP: 0.47 m x 0.47 m x 0.002 m Mass of each SAP: 1.24 Kg Material: aluminium Euler Modulus: $7 \cdot 10^{10} \text{ N/m}^2$ density: 2810 Kg/m^3 Poisson ratio: 0.33

Table 4.2: Actuators specifications

	Specifications
Robotic arm actuators	Maximum torque: 0.25 Nm
Reaction Wheels	Max. spin rate: 6000 rpm Max. angular momentum: 0.45 Nms Max. angular acceleration: 300 rpm/s Moments of inertia: $7.16 \cdot 10^{-4} \text{ Kg/m}^2$ Max. torque: 0.0225 Nm

4.2 Simulation environment

All the phases of modelling and simulation are performed in MATLAB/SIMULINK environment, with a sample time $\Delta t = 0.001s$, and the differential equations are solved with the Runge-Kutta ode4 solver. In Fig. 4.1 the block scheme in Simulink is presented. There are three main subsystems:

- The manipulator dynamics subsystem, that includes the equation of motion of the robotic arm. The input is the control torque from the PID controller, and the output are the joint angles θ_1, θ_2 .
- The PID controller subsystem, that receives in input the joint angles from the manipulator plant, and provides the manipulator's control torques in output.
- The most complex subsystem is the attitude dynamics and control subsystem. It includes the spacecraft attitude dynamics and kinematics, through the Euler equations and quaternions, the solar panels' dynamics, and the ADRC/LQR controller for attitude control. This subsystem receives in input the external disturbance of the manipulator, while gives in output the Euler angles and the quaternions.

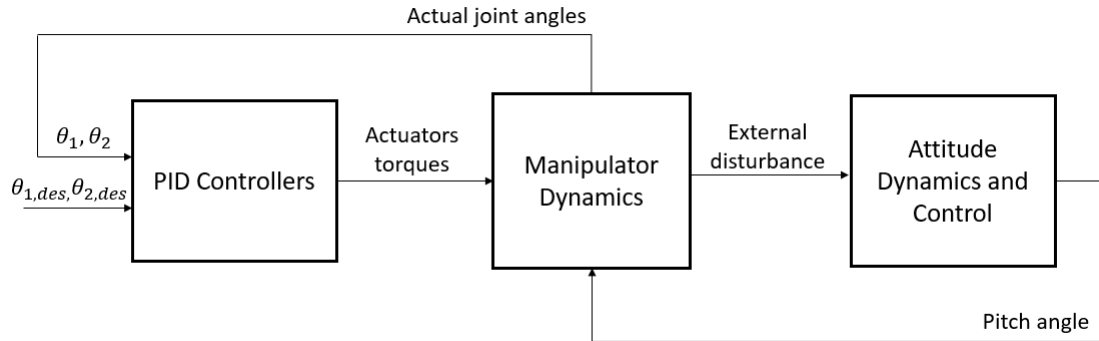


Figure 4.1: Spacecraft block scheme in Simulink

4.3 Robotic manipulator results

The robotic manipulator motion and the PID action in Fig. 4.2 are studied for the specific mission scenario of the spacecraft that has reached the desired attitude configuration and moves the robotic arm. It can be observed that, when one of the two links moves to reach the desired joint angle, the actuators of the other link exert a torque in order to maintain the angular position. This occurs, for example, after 40 s: the second link moves to reach the angular position $\theta_2 = 20^\circ$, and exerts a disturbance torque on the first link that, thanks to the PID controller, can return to the desired angle. Moreover, in Fig. 4.3 the saturation of the actuators torque is equal to 0.25 Nm . The PID gains for both links are in Tab. 4.3. Both the two PID controllers provide a stable response, with no overshoot and a rise time of about 3 s.

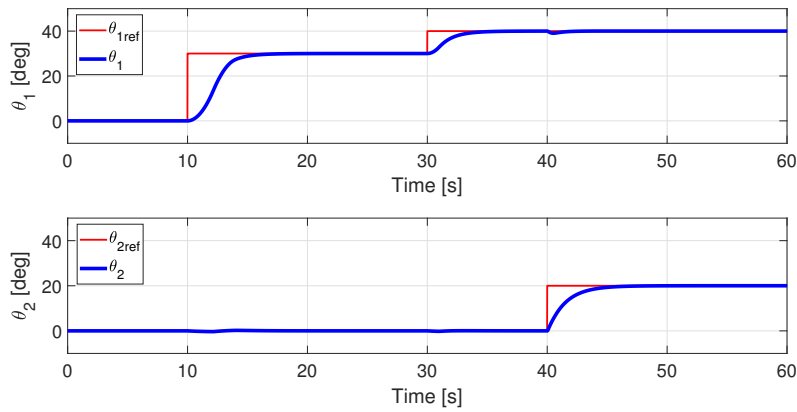


Figure 4.2: Robotic manipulator motion

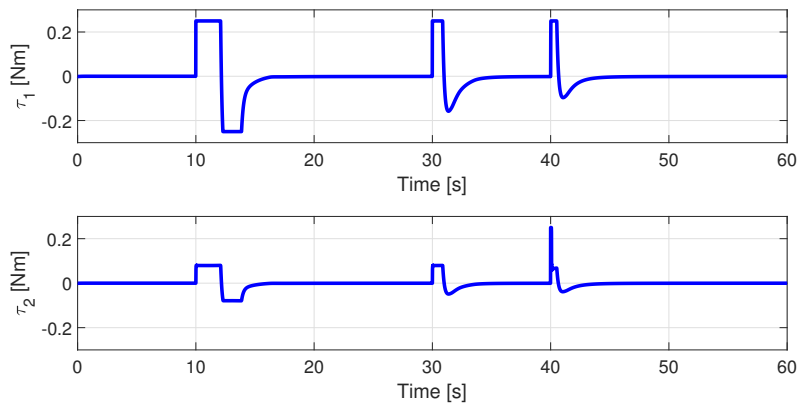


Figure 4.3: Robotic manipulator actuators toques

Table 4.3: PID controller gains

	Link 1	Link 2
k_P	15	10
k_I	0.001	0.001
k_D	20	15

4.4 Flexible solar panels results

For the flexible solar panels dynamics, a FEM analysis is performed in order to evaluate the natural frequencies and modes, and the eigenvectors matrix used in the model. The FEM analysis is conducted with PATRAN and NASTRAN software. The four solar panels are modelled in Patran as aluminium plates, and a modal analysis is performed. After that, the frequencies and eigenvectors obtained from the analysis are used in the simulation. A code is written in MATLAB to evaluate all the matrices in the dynamics equation of the flexible part, and the δ coupling matrices defined in Chapter 2 are computed.

This section is divided in two parts: firstly, the FEM analysis results are reported, and then the simulation results are discussed.

4.4.1 FEM analysis results

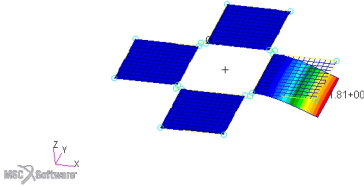
The results obtained from the FEM analysis in terms of frequencies and normal modes for each solar panel are shown in Tab. 4.4 and Figures 4.4, 4.5 and 4.6. The first three normal modes have been evaluated with the modal analysis in PATRAN/NASTRAN: the first and third are bending modes, while the second one is a torsional mode. For the computation of the coupling matrices δ_i , for $i = 1, \dots, 4$, the first two bending modes have been taken into account.

Table 4.4: PID controller gains

	Natural frequency [rad/s]	Damping
Mode 1	48.2283	0.0482
Mode 2	118.1524	0.1182
Mode 3	295.7264	0.2957

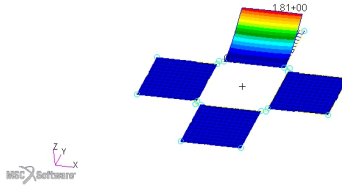
4 – Simulation results

Patran 2019 (Student Edition) 04-Dec-20 10:19:22
 Fringe: Default, A1.Mode 1: Freq. = 7.5881, Eigenvectors, Translational, Magnitude, (NON-LAYERED)
 Deform: Default, A1.Mode 1: Freq. = 7.5881, Eigenvectors, Translational,



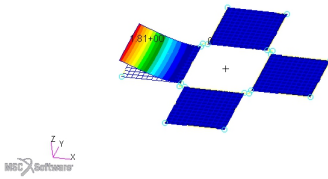
(a) *First solar panel mode.*

Patran 2019 (Student Edition) 04-Dec-20 10:21:01
 Fringe: Default, A1.Mode 2: Freq. = 7.5881, Eigenvectors, Translational, Magnitude, (NON-LAYERED)
 Deform: Default, A1.Mode 2: Freq. = 7.5881, Eigenvectors, Translational,



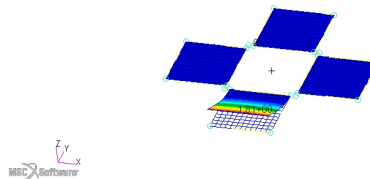
(b) *Second solar panel mode.*

Patran 2019 (Student Edition) 04-Dec-20 10:21:40
 Fringe: Default, A1.Mode 3: Freq. = 7.5881, Eigenvectors, Translational, Magnitude, (NON-LAYERED)
 Deform: Default, A1.Mode 3: Freq. = 7.5881, Eigenvectors, Translational,



(c) *Third solar panel mode.*

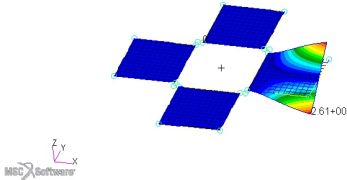
Patran 2019 (Student Edition) 04-Dec-20 10:22:02
 Fringe: Default, A1.Mode 4: Freq. = 7.5881, Eigenvectors, Translational, Magnitude, (NON-LAYERED)
 Deform: Default, A1.Mode 4: Freq. = 7.5881, Eigenvectors, Translational,



(d) *Fourth solar panel mode.*

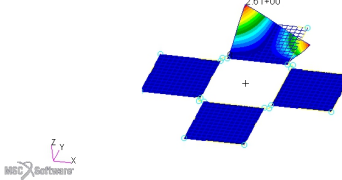
Figure 4.4: Mode 1.

Patran 2019 (Student Edition) 04-Dec-20 10:22:43
 Fringe: Default, A1.Mode 6: Freq. = 18.206, Eigenvectors, Translational, Magnitude, (NON-LAYERED)
 Deform: Default, A1.Mode 6: Freq. = 18.206, Eigenvectors, Translational,



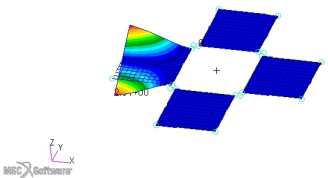
(a) *First solar panel mode.*

Patran 2019 (Student Edition) 04-Dec-20 10:23:12
 Fringe: Default, A1.Mode 8: Freq. = 18.206, Eigenvectors, Translational, Magnitude, (NON-LAYERED)
 Deform: Default, A1.Mode 8: Freq. = 18.206, Eigenvectors, Translational,



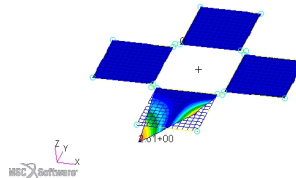
(b) *Second solar panel mode.*

Patran 2019 (Student Edition) 04-Dec-20 10:23:00
 Fringe: Default, A1.Mode 7: Freq. = 18.206, Eigenvectors, Translational, Magnitude, (NON-LAYERED)
 Deform: Default, A1.Mode 7: Freq. = 18.206, Eigenvectors, Translational,



(c) *Third solar panel mode.*

Patran 2019 (Student Edition) 04-Dec-20 10:22:32
 Fringe: Default, A1.Mode 5: Freq. = 18.206, Eigenvectors, Translational, Magnitude, (NON-LAYERED)
 Deform: Default, A1.Mode 5: Freq. = 18.206, Eigenvectors, Translational,



(d) *Fourth solar panel mode.*

Figure 4.5: Mode 2.

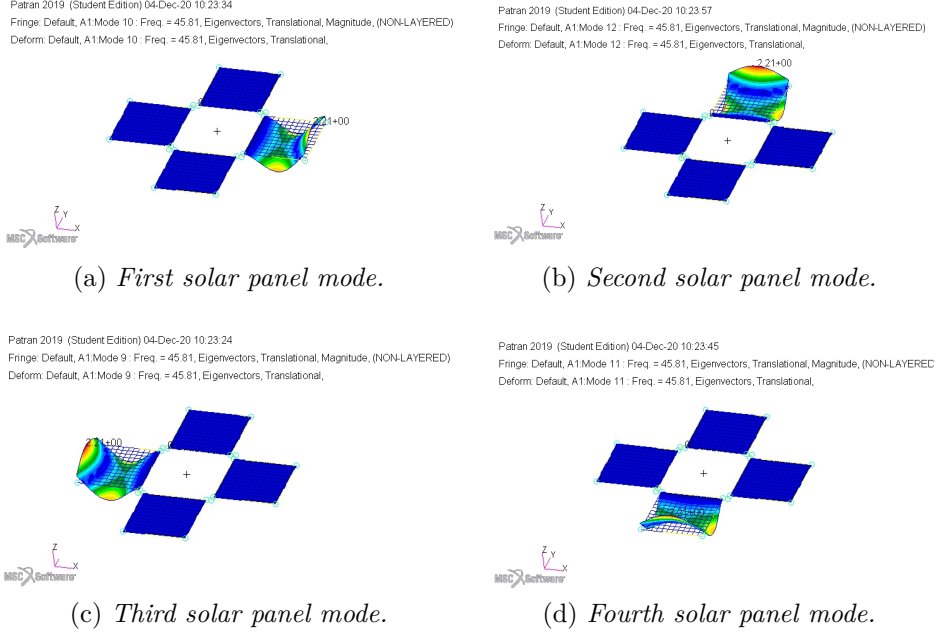


Figure 4.6: Mode 3.

4.4.2 Solar panels simulation results

The values of natural frequencies in Tab. 4.4 are used to compute the stiffness matrix \mathbf{K} and the damping matrix \mathbf{C} , for $\gamma = 0.002$. Knowing the damping matrix, the damping values in Tab. 4.4 can be obtained.

From the modal analysis, the eigenvectors for the sub-panels of each solar panel are evaluated. Hence, the four $N \times 3$ coupling matrices between the rigid hub and the flexible solar panels are obtained, with $N = 2$, equal to the number of shape modes:

$$\delta_1 = \begin{bmatrix} 0 & -0.5305 & 0 \\ 0 & -0.1901 & 0 \end{bmatrix} \sqrt{Kg/m^2}$$

$$\delta_2 = \begin{bmatrix} 0 & 0 & -0.5404 \\ 0 & 0 & 0.1817 \end{bmatrix} \sqrt{Kg/m^2}$$

$$\delta_3 = \begin{bmatrix} 0 & -0.5305 & 0 \\ 0 & 0.1901 & 0 \end{bmatrix} \sqrt{Kg/m^2}$$

$$\delta_4 = \begin{bmatrix} 0 & 0 & 0.5404 \\ 0 & 0 & -0.1817 \end{bmatrix} \sqrt{Kg/m^2}$$

Two mission scenarios are presented in order to evaluate the internal disturbance due to the flexible solar panels. A first simulation is performed when the spacecraft is in the desired attitude and moves the robotic arm, as in section 4.3. The results of this simulation are shown in Fig. 4.7. It can be observed a vibration of the solar panels due to their flexibility when the movement of the manipulator occurs. Because of the damping coefficient included in the model, this vibration is damped in a few seconds. In this case the disturbance torque of the panels affects just the pitch axis, due to the movement of the robotic arm in the xz plane.

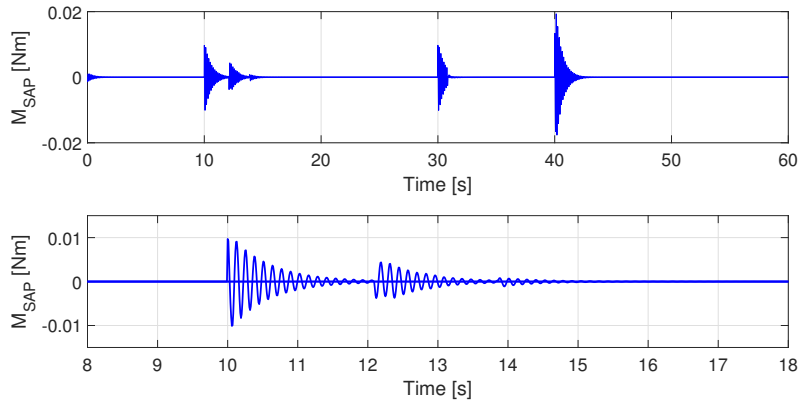


Figure 4.7: Solar panels disturbance torque

The second simulation starts with an initial quaternion $\mathbf{q}_0 = [0.5, 0.5, 0.5, 0.5]^T$, and a desired quaternion $\mathbf{q}_{des} = [1, 0, 0, 0]^T$. Note that, in this case, a disturbance on the yaw axis occurs too, due to the attitude manoeuvre, as shown in Fig. 4.8. The disturbance on z axis is two order of magnitude lower than the torque on y axis, due the influence of the robotic arm that represents the higher disturbance acting on the spacecraft. The disturbance torque on the z axis is higher in the first seconds of the simulation, when the spacecraft starts to move towards the desired attitude.

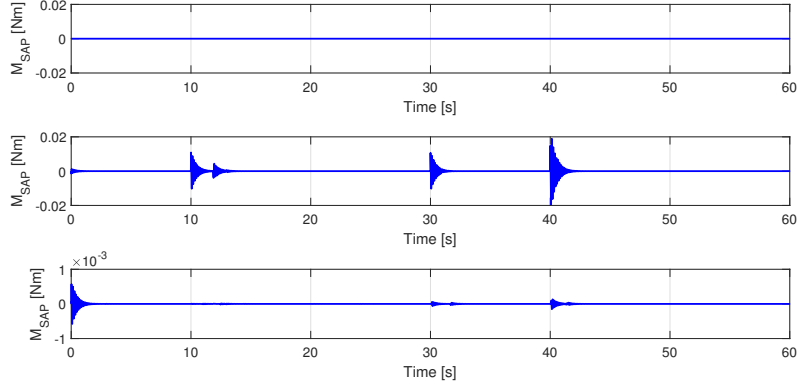


Figure 4.8: Solar panels disturbance torque during an attitude manoeuvre

4.5 Attitude control results

This section is organised as follows: the attitude results in terms of quaternions and Euler angles are reported in the general case of the spacecraft with an initial quaternion $\mathbf{q}_0 = [0.5, 0.5, 0.5, 0.5]^T$ that reaches the desired quaternion $\mathbf{q}_{des} = [1, 0, 0, 0]^T$. To obtain this result, a tuning of all the parameters of the two attitude controllers was required. Firstly the attitude results are discussed without the external disturbance of the manipulator. Subsequently, the manipulator's disturbance is added to the model, and the results are argued. After that, a section is dedicated to the discussion of the parameters tuning of the two controllers. Finally, a comparison between the ADRC/LQR controller implemented in this thesis and a simple LQR for attitude control is provided to analyse the advantages of the disturbance rejection.

4.5.1 Attitude control without the manipulator movement

The simulation starts with an initial quaternion $\mathbf{q}_0 = [0.5, 0.5, 0.5, 0.5]^T$. The desired quaternion is $\mathbf{q}_{des} = [1, 0, 0, 0]^T$. The system of the four reaction wheels is in a pyramidal configuration, with $\alpha = 0^\circ$ and $\beta = 30^\circ$. For the definition of these angles, refer to Fig. 2.4 in section 2.1.2. The system of actuators is characterized by a torque limitation of 0.0225 Nm and a maximum angular momentum of 0.45 Nm s , as in the specifications of PROCYON spacecraft. The parameter of the low pass filter used in the reaction wheels model is assumed to be $\tau_{RW} = 1$.

In Figures 4.9, 4.10 and 4.11 the quaternions, Euler angles and angular velocity responses are shown. It can be observed the achievement of the desired attitude around 150 s. In Fig. 4.12, the reaction wheels torques required for the attitude manoeuvre are shown, in particular the repartition of the torques provided by each of the four reaction wheels on the three axes.

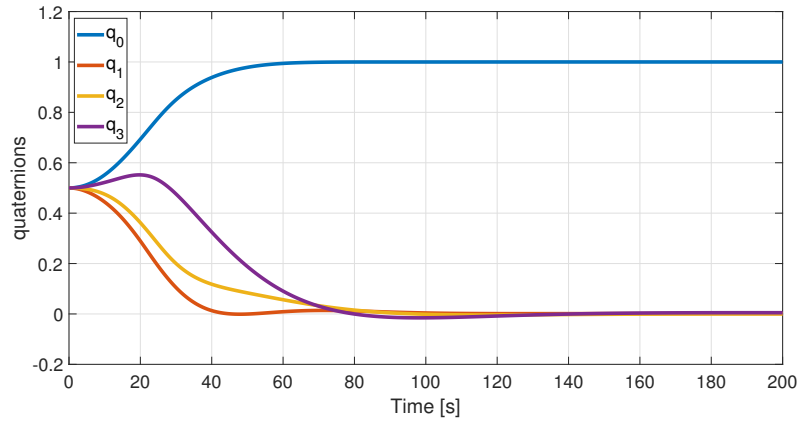


Figure 4.9: Quaternions response without the manipulator disturbance

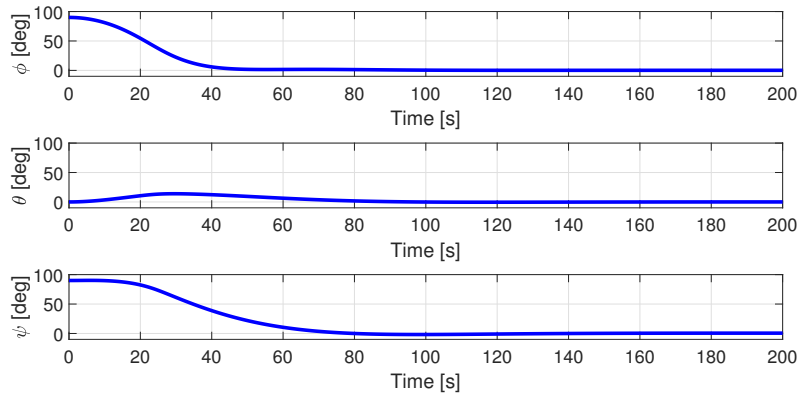


Figure 4.10: Euler angles without the manipulator disturbance

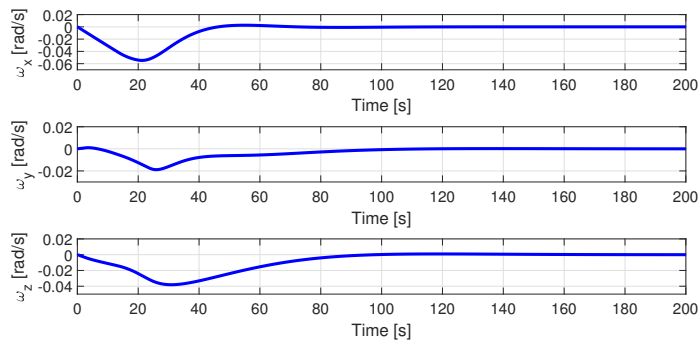


Figure 4.11: Angular velocity without the manipulator disturbance

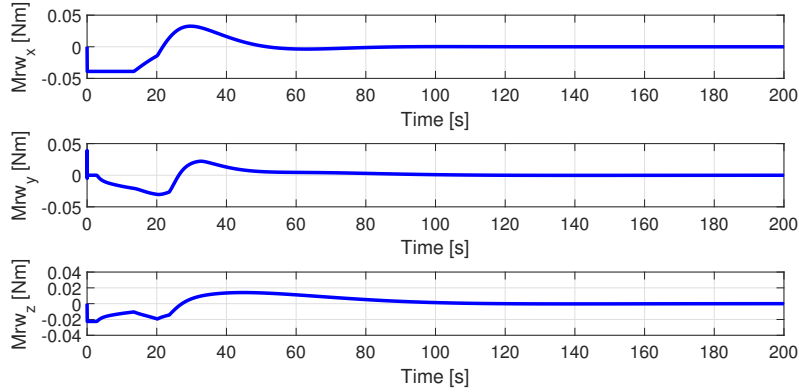


Figure 4.12: RWs torque commands without the manipulator disturbance

4.5.2 Attitude control with the manipulator movement

In this section the general case of the spacecraft reaching the desired attitude $\mathbf{q}_{des} = [1, 0, 0]^T$ during the movement of the robotic arm is argued. It is interesting to note the influence of the robotic arm on the spacecraft attitude. In this thesis the external disturbance of the manipulator is the higher disturbance acting on the spacecraft, and for this reason a particular attention is given to the control of the pitch angle, as discussed in the next section. For the sake of completeness, the gravity gradient external disturbance has been evaluated to demonstrate the lower order of magnitude of this torque, equal to $10^{-5} Nm$ with respect to the solar panels internal disturbance (Fig. 4.7) and the manipulator disturbance (Fig. 4.3). In Fig. 4.13, the gravity gradient torque is shown.

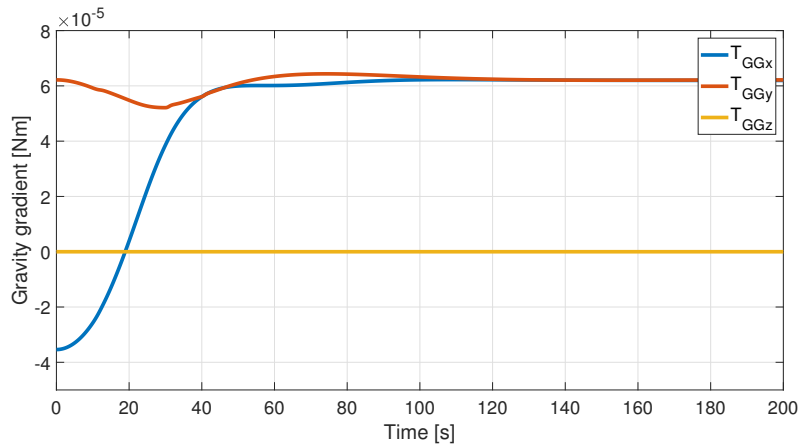


Figure 4.13: Gravity gradient torque

The results regarding the quaternions, Euler angles, angular velocity and reaction wheels torques are reported in the next figures. It can be observed that the disturbance of the robotic manipulator is evident in the results. Thanks to the ADRC/LQR controller the spacecraft is capable to contrast this high disturbance and takes the spacecraft to the desired attitude. In this simulation the following movement of the manipulator is performed, as in Fig. 4.2: after 10 s the first link starts moving towards the desired joint angle of 30° , and then reaches 40° after 30 s, while the second link reaches 20° after the command given at 40 s. It is evident how the reaction wheels react to the movement of the arm, and provide the required torque in order to correct the attitude and reject the disturbance.

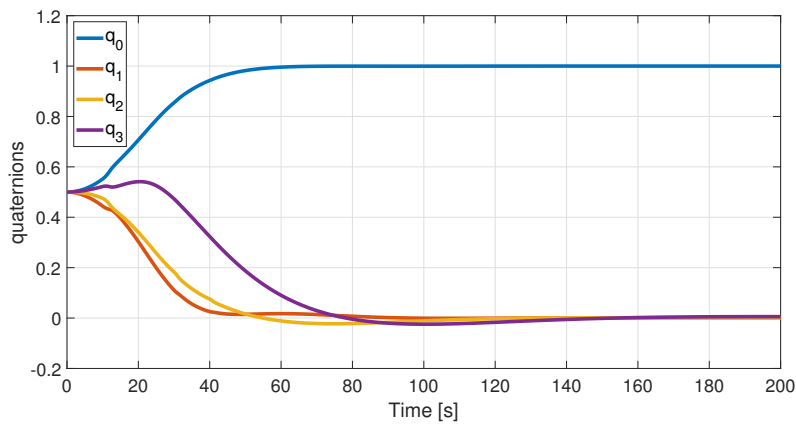


Figure 4.14: Quaternions response with the manipulator disturbance

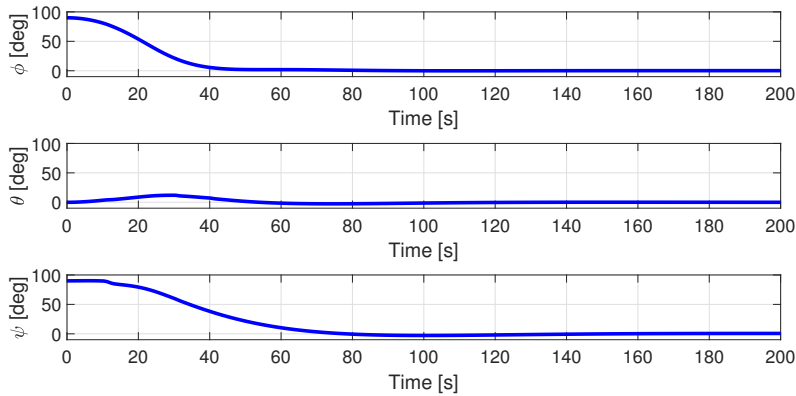


Figure 4.15: Euler angles with the manipulator disturbance

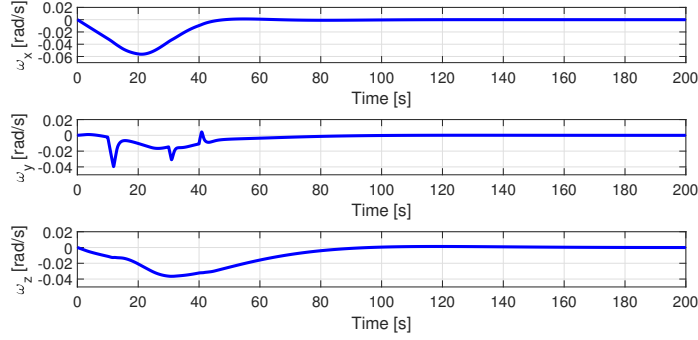


Figure 4.16: Angular velocity with the manipulator disturbance

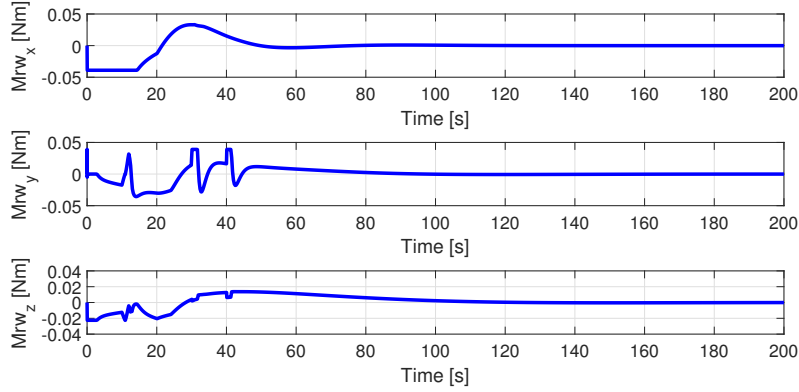


Figure 4.17: RWs torque commands with the manipulator disturbance

4.5.3 ADRC/LQR parameters tuning

This section is reserved to the parameters chosen for ADRC/LQR. The weighting matrices for the Linear Quadratic Regulator are given by:

$$\mathbf{Q} = \text{diag}([1, 0.1, 1, 0.01, 0.01, 0.01]) \cdot 10^{-6}$$

$$\mathbf{R} = \text{diag}([0.08, 0.05, 0.8]) \cdot 10^{-3}$$

The fundamental part of the ADRC/LQR tuning was the choice of the TD and ESO coefficients. In this work three different TD and ESO systems are considered for each Euler angle, due to the adaptability of the ADRC to MIMO systems. In Tab. 4.5 all the coefficients used for ADRC controller are resumed.

Table 4.5: Parameters of ADRC

	ϕ	θ	ψ
Tracking Differentiator	$r = 5$	$r = 5$	$r = 5$
	$a_1 = 0.5$	$a_1 = 0.5$	$a_1 = 0.5$
	$a_2 = 0.25$	$a_2 = 0.25$	$a_2 = 0.25$
	$h = 0.001$	$h = 0.001$	$h = 0.001$
Extended State Observer	$b_0 = 0.0799$	$b_0 = 0.0618$	$b_0 = 0.0618$
	$\beta_1 = 200$	$\beta_1 = 120$	$\beta_1 = 200$
	$\beta_2 = 100$	$\beta_2 = 4800$	$\beta_2 = 100$
	$\beta_3 = 0.001$	$\beta_3 = 64000$	$\beta_3 = 0.001$

The parameters of the ADRC are adjusted until a satisfactory response from the controller is obtained. The objective of this type of controller is the estimation of the states of the system, and in particular the total disturbance. As discussed in Chapter 3, the states x_1 and x_2 are respectively the Euler angles and its derivatives, while x_3 is the total disturbance, defined by the variable f . The output of the Extended State Observer z_1, z_2 , and z_3 follow respectively x_1, x_2 , and x_3 . The tracking of the three states for each axis is observed in the following figures. In detail, the black lines are the actual states of the system, while the red dashed lines are the estimated states.

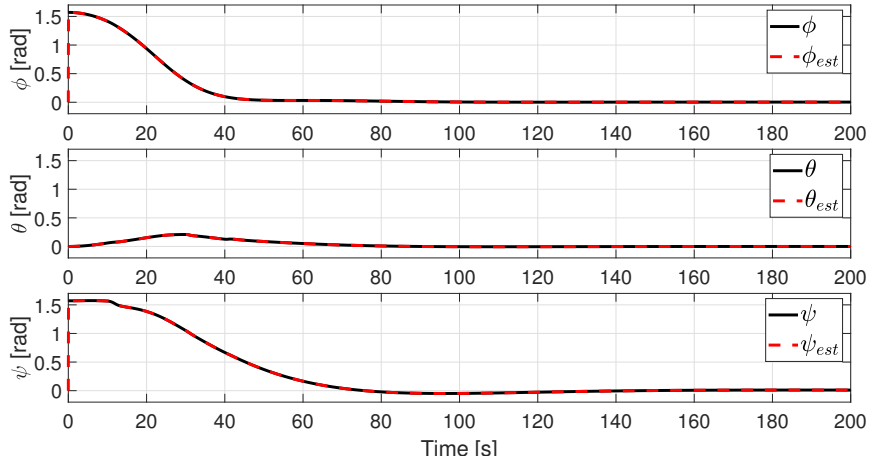


Figure 4.18: Estimation of Euler angles with ESO.

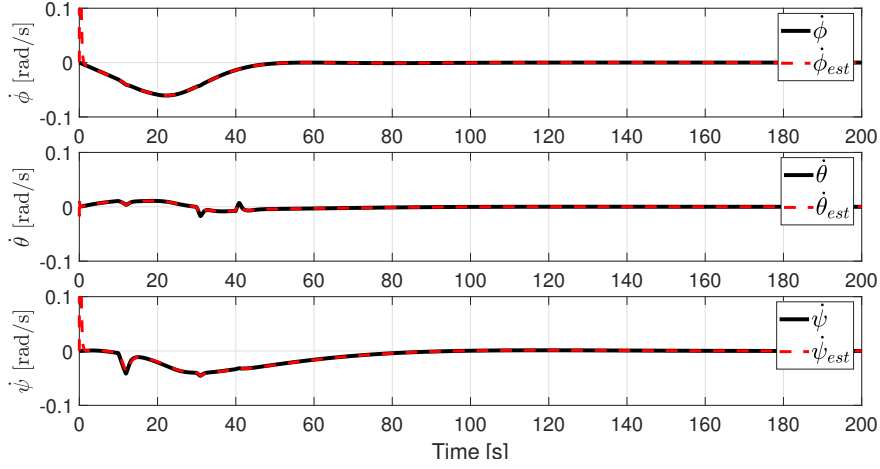
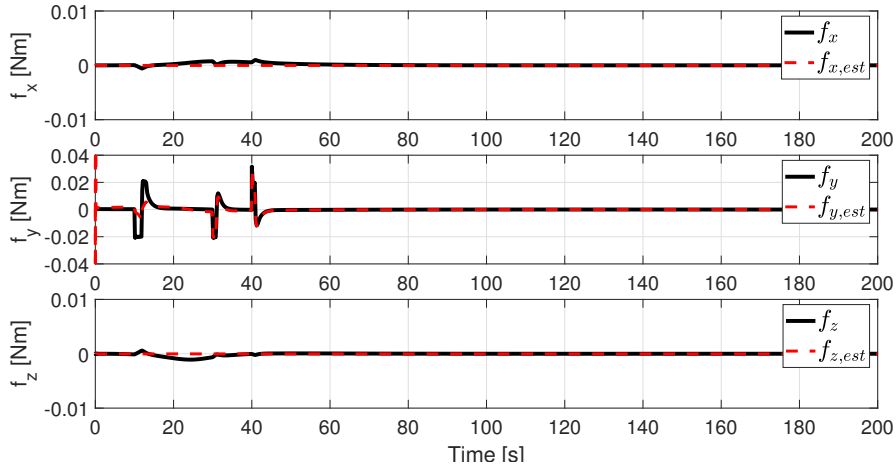


Figure 4.19: Estimation of Euler angles derivatives with ESO.

Figure 4.20: Estimation of total disturbance f with ESO.

As can be seen in Figures 4.18 and 4.19, the states z_1 and z_2 , represented by the red dashed lines, are able to estimate the Euler angles and the relative derivative terms. The results in Fig. 4.20 are the most significant in terms of the estimation of the total disturbance of the system that has to be rejected. As has already been said, in this work the attention is focused especially on the pitch axis, due to the high disturbance that affect the pitch attitude. For this reason, the coefficients of the ESO system should be suitably chosen to obtain an optimal response from the z_3 variable. Referring to the estimation of f_y in Fig. 4.20, the controller starts with a non-zero initial condition set in the integrator, and tries to track the signal of the total disturbance on the pitch axis. First, the signal and its estimation are not coincident as in the case of z_1 and z_2 , but subsequently the controller is able to track

the signal quickly. The fast tracking response is subjected to the correct tuning of all the ADRC parameters, that can be adjusted to obtain a better response since the first seconds of the simulation.

4.5.4 Comparison of ADRC/LQR and LQR controllers

A final comparison between the ADRC/LQR controller implemented in this thesis and a simple LQR is provided in order to verify the improvement of the results when the disturbance rejection is included in the model, through the Extended State Observer. In the following figures the comparison of the two types of controllers in terms of quaternions and Euler angles is shown. In Tab. 4.6 the time domain specifications of the ADRC/LQR and the LQR controllers are compared. The ADRC/LQR controller reaches the desired attitude with a faster response compared to the LQR controller in the case of the pitch and yaw angles. Referring to the Figures 4.25, 4.26 and 4.27, the ADRC/LQR controller is able to reject better the disturbance due to the manipulator motion, and it tries also to reduce the overshoot that can be observed in the LQR response, In detail, for the pitch dynamics an overshoot occurs at 30 s, as shown in Fig. 4.26. The roll control with the LQR performs better than the ADRC/LQR for the rising time, but it has a slower response, a greater settling time, and an overshoot of 3%. The pitch control is the most critical parameter in this thesis, and, thanks to the ADRC/LQR, a satisfactory response is obtained, although the higher overshoot in the first 30 s. The disturbance rejection combined with the LQR acts better for the yaw control compared to the LQR, with a good performance in terms of rising and settling time, at the cost of a small overshoot.

Table 4.6: Resulting time responses of ADRC/LQR and LQR

	Euler angles	Rising time [s]	Settling time [s]	Steady-states error	Overshoot
ADRC/LQR	ϕ	26.57	64.02	0	0
	θ	4.31	50.08	0	21%
	ψ	43	121.8	0	3%
LQR	ϕ	23.34	69.47	0	3%
	θ	2.05	88.04	0	0
	ψ	63.1	135.9	0	0

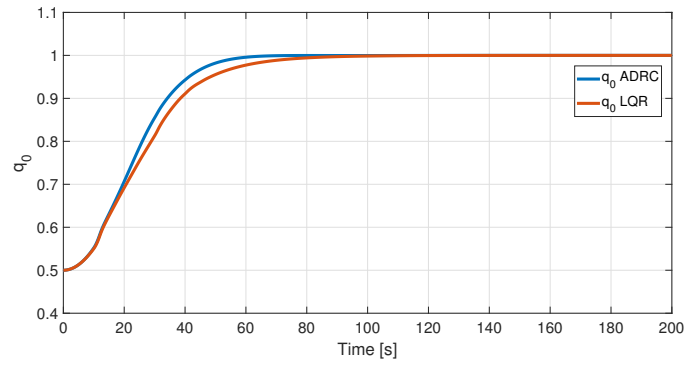


Figure 4.21: Comparison of q_0 .

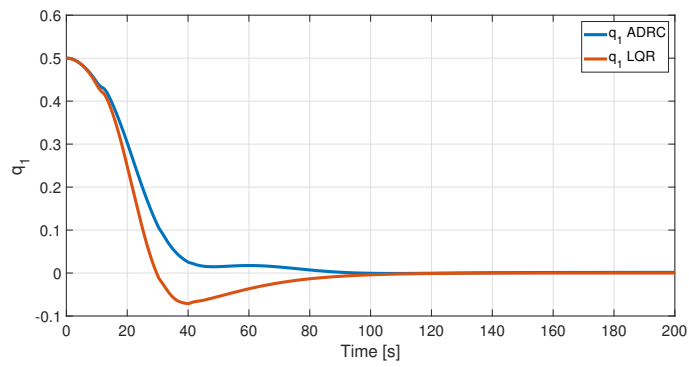


Figure 4.22: Comparison of q_1 .

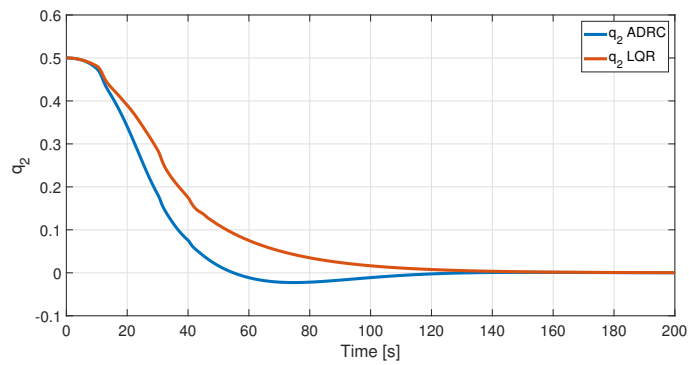


Figure 4.23: Comparison of q_2 .

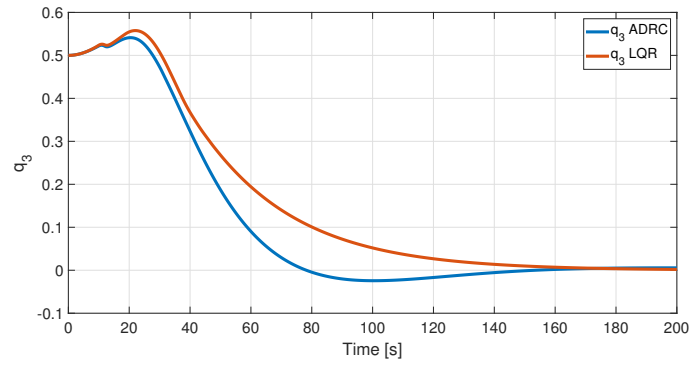


Figure 4.24: Comparison of q_3 .

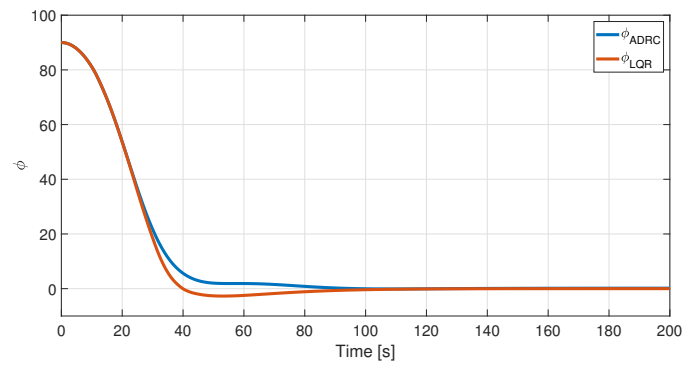


Figure 4.25: Comparison of ϕ .

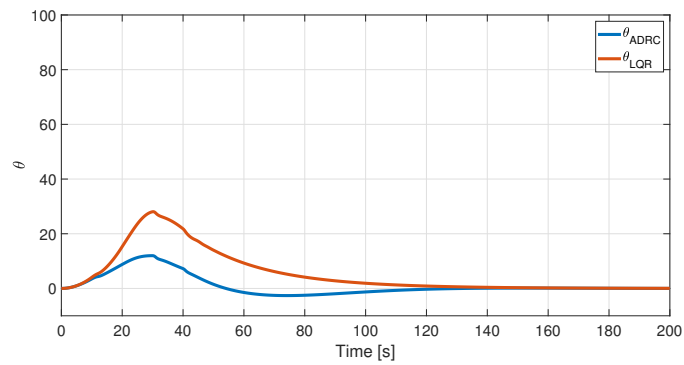
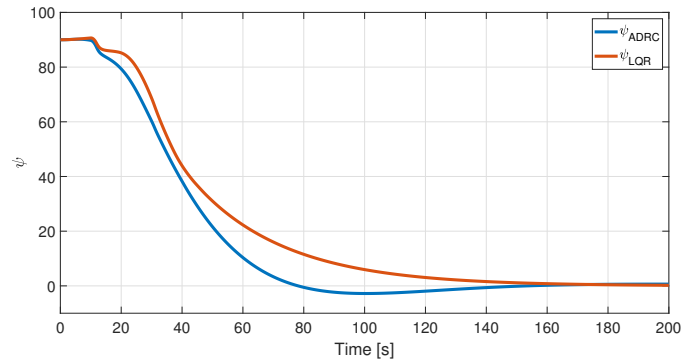


Figure 4.26: Comparison of θ .

Figure 4.27: Comparison of ψ .

4.6 CAD model and animations

The last part of this chapter is relative to the CAD model realized with SolidWorks software, and the animations obtained with the 3D World Editor tool of MATLAB/SIMULINK. This work was useful in order to have a 3D animation of the manoeuvres performed by the spacecraft, for example the simulation of the deployment of the solar panels, the achievement of the desired attitude, and the deployment of the robotic manipulator. In Fig. 4.29 the CAD models of the spacecraft are shown. The CAD has been imported in the 3D World Editor tool, and connected to the model in the SIMULINK environment through the VR Sink block (Figures 4.28).

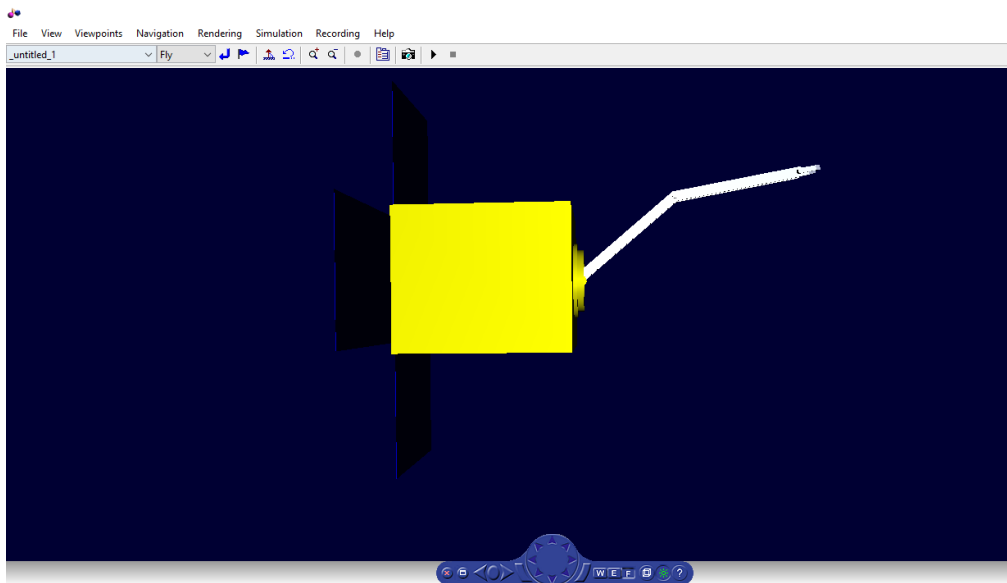


Figure 4.28: VR Sink block graphics interface.

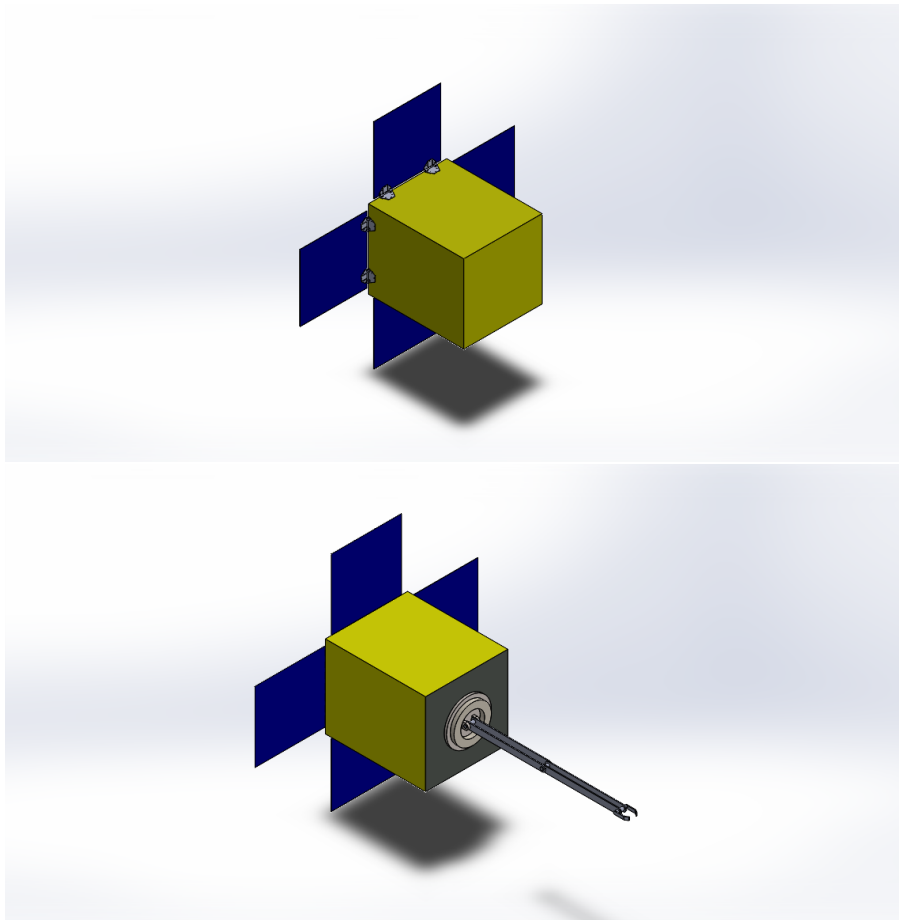


Figure 4.29: Spacecraft CAD model

Chapter 5

Conclusions and future works

This thesis aims at developing the dynamics and control model of a flexible spacecraft with a robotic manipulator, taking the JAXA PROCYON satellite as the main body of the spacecraft. Different tasks are dealt with in this work: the manipulator dynamics and control model for in-orbit servicing, such as the space debris capture, the dynamics of flexible solar panels, and the implementation of the attitude control strategy. First, a hybrid approach is chosen for studying the robotic arm and the spacecraft dynamics. In particular, the Lagrangian formulation is used to obtain the equation of motion of the manipulator, while the attitude dynamics is studied through the Euler equation, including the reaction wheels and the solar panels' model. A PID controller is used for the manipulator control to achieve the desired joint angles. The results obtained are satisfactory and ensure a fast and stable response. In order to have a complete and accurate model of the spacecraft, the flexible solar panels have been studied through a modal analysis with PATRAN/-NASTRAN. The natural frequencies and eigenvectors obtained have been used for the implementation of the flexible panels' model in MATLAB/SIMULINK. In this thesis, the evaluation of the coupling matrix between the rigid hub and the flexible appendages is found, together with the stiffness and damping matrices for the specific solar panels of PROCYON spacecraft. Thanks to this analysis, the disturbance torque due to the vibration of the flexible panels is studied and controlled. Furthermore, the final and main task of this work is the development of a GNC system for flexible spacecraft. Particular attention is focused on the implementation of an attitude control strategy capable of rejecting all the disturbances acting on the spacecraft and ensuring a good performance. The spacecraft is subjected to the high disturbance of the robotic manipulator, which has an order of magnitude greater than the vibration of the solar panels and the other external disturbances. For this purpose, the combination of the LQR controller and the ADRC strategy is taken

into account to contrast the internal and external disturbances, with the optimal behaviour of the LQR controller. Three different ADRC systems are considered for each Euler angle, including a Tracking Differentiator and an Extended State Observer for the estimation of the states and the total disturbance of the system. The pitch control is studied with particular attention due to the disturbance of the arm acting on this axis. The results show that the ADRC/LQR controller performs better than the traditional LQR, in particular for the pitch and yaw control, justifying the combined use of the two controllers for the disturbance rejection.

Possible future works are relative to the development of a more accurate model of the robotic manipulator, including the end effector movement, and a trajectory tracking algorithm for the target/debris capture. Moreover, the position dynamics and control can be implemented, together with the attitude dynamics, to have a complete model of the spacecraft. Finally, the ADRC algorithm requires a good knowledge of all the parameters involved, hence a more detailed study of the optimal response from this type of controller can be interesting to further explore.

Bibliography

- [1] Yang Gao and Steve Chien. “Review on space robotics: Toward top-level science through space exploration”. In: *Science Robotics* 2 (June 2017), eaan5074. DOI: [10.1126/scirobotics.aan5074](https://doi.org/10.1126/scirobotics.aan5074).
- [2] Dr. Jason Forshaw. *How Can We Fix The Space Junk Problem? A Net And A Harpoon, Say Aerospace Engineers*. <https://www.ge.com/news/reports/can-fix-space-junk-problem-net-harpoon-say-aerospace-engineers>. 15 May 2017.
- [3] *OSIRIS-REx*. <https://www.nasa.gov/osiris-rex>. NASA.
- [4] Paul Keaveny. *NASA’s Curiosity heads for Mars, and opens a new chapter for humankind*. <https://theconversation.com/nasas-curiosity-heads-for-mars-and-opens-a-new-chapter-for-humankind-4164>. The Conversation/Science+Technology. 2011.
- [5] J. Sasiadek. “Space Robotics and its Challenges”. In: (Feb. 2019).
- [6] Alex Ellery. “Tutorial Review on Space Manipulators for Space Debris Mitigation”. In: *Robotics* 8 (Apr. 2019), p. 34. DOI: [10.3390/robotics8020034](https://doi.org/10.3390/robotics8020034).
- [7] Panfeng Huang et al. “Chapter 1 - Introduction”. In: *Tethered Space Robot*. Ed. by Panfeng Huang et al. Academic Press, 2018, pp. 1–26. ISBN: 978-0-12-812309-6. DOI: <https://doi.org/10.1016/B978-0-12-812309-6.00001-4>. URL: <https://www.sciencedirect.com/science/article/pii/B9780128123096000014>.
- [8] Kazuya Yoshida and Brian Wilcox. “Space Robots and Systems”. In: *Springer Handbook of Robotics*. Ed. by Bruno Siciliano and Oussama Khatib. Berlin, Heidelberg: Springer Berlin Heidelberg, 2008, pp. 1031–1063. ISBN: 978-3-540-30301-5. DOI: [10.1007/978-3-540-30301-5_46](https://doi.org/10.1007/978-3-540-30301-5_46). URL: https://doi.org/10.1007/978-3-540-30301-5_46.
- [9] Angel Flores-Abad et al. “A review of space robotics technologies for on-orbit servicing”. In: *Progress in Aerospace Sciences* 68 (2014), pp. 1–26. ISSN: 0376-0421. DOI: <https://doi.org/10.1016/j.paerosci.2014.03.002>. URL: <https://www.sciencedirect.com/science/article/pii/S0376042114000347>.

- [10] J. D. MacNaughton. “A Review of the Canadian Space Program”. In: *The Space Congress® Proceedings. 4* (1980).
- [11] Martha E. Demeo. “Remote Manipulator System (RMS)-based Controls-Structures Interaction (CSI) flight experiment feasibility study”. In: 1990.
- [12] NASA. *Payload bay activity during second EVA of STS-72 mission*. <https://archive.org/details/STS072-722-041>. Internet Achieve. 1996.
- [13] MICHAEL SCOTT, MICHAEL GILBERT, and MARTHA DEMEO. “Active vibration damping of the Space Shuttle Remote Manipulator System”. In: *Navigation and Control Conference*. DOI: [10.2514/6.1991-2621](https://doi.org/10.2514/6.1991-2621). eprint: <https://arc.aiaa.org/doi/pdf/10.2514/6.1991-2621>. URL: <https://arc.aiaa.org/doi/abs/10.2514/6.1991-2621>.
- [14] *Flight History of Canadarm*. <https://www.asc-csa.gc.ca/eng/canadarm/flight.asp>. Canada Space Agency. 7 November 2011.
- [15] *Historic First Moves*. <https://www.asc-csa.gc.ca/eng/canadarm/beginning.asp>. Canada Space Agency. 28 October 2011. Retrieved 27 October 2012.
- [16] Graham Gibbs and Savi Sachdev. “Canada and the International Space Station program: Overview and status”. In: *Acta Astronautica* 51.1 (2002), pp. 591–600. ISSN: 0094-5765. DOI: [https://doi.org/10.1016/S0094-5765\(02\)00077-2](https://doi.org/10.1016/S0094-5765(02)00077-2). URL: <https://www.sciencedirect.com/science/article/pii/S0094576502000772>.
- [17] Nancy Currie-Gregg and Brian Peacock. “International Space Station Robotic Systems Operations - a Human Factors Perspective”. In: *Proceedings of the Human Factors and Ergonomics Society Annual Meeting* 46 (Sept. 2002). DOI: [10.1177/154193120204600106](https://doi.org/10.1177/154193120204600106).
- [18] *Canadarm2 robotic arm*. https://www.esa.int/ESA_Multimedia/Images/2020/04/Canadarm2_robotic_arm. ESA/Science& Exploration. 2020.
- [19] Mark Garcia. *Special Purpose Dexterous Manipulator*. https://www.nasa.gov/mission_pages/station/structure/elements/special-purpose-dextrous-manipulator/. NASA. 2018.
- [20] Adrienne Alessandro. *NASA’s Successful Robotic Refueling Demo Points To a Bright Satellite-Servicing Future*. https://www.nasa.gov/mission_pages/station/research/news/rrm_success.html. NASA’s Goddard Space Flight Center. 2 August 2013.
- [21] Doi S. Sato N. “JEM remote manipulator system (JEMRMS) human-in-the-loop test”. In: *The 22nd international symposium on space technology and science* (2000). Morioka, Japan, pp. 1195–9.

- [22] NASA. *NanoRacks CubeSat Launch*. https://upload.wikimedia.org/wikipedia/commons/1/13/NanoRacksCubeSatLaunch_ISS038-E-056389.jpg. 2014.
- [23] R. Boumans and C. Heemskerk. “The European Robotic Arm for the International Space Station”. In: *Robotics and Autonomous Systems* 23.1 (1998). Space Robotics in Europe, pp. 17–27. ISSN: 0921-8890. DOI: [https://doi.org/10.1016/S0921-8890\(97\)00054-7](https://doi.org/10.1016/S0921-8890(97)00054-7). URL: <https://www.sciencedirect.com/science/article/pii/S0921889097000547>.
- [24] ESA. *European Robotic Arm (ERA) during flat floor testing*. [https://www.esa.int/ESA_Multimedia/Missions/European_Robot_Arm_ERA/\(result_type\)/images](https://www.esa.int/ESA_Multimedia/Missions/European_Robot_Arm_ERA/(result_type)/images). Science & Exploration. 2006.
- [25] G. Hirzinger et al. “ROTEX—the first remotely controlled robot in space”. In: *Proceedings of the 1994 IEEE International Conference on Robotics and Automation*. 1994, 2604–2611 vol.3. DOI: [10.1109/ROBOT.1994.351121](https://doi.org/10.1109/ROBOT.1994.351121).
- [26] G. Visentin and F. Didot. “TESTING SPACE ROBOTICS ON THE JAPANESE ETS-VII SATELLITE”. In: 1999.
- [27] *ETS-VII (Engineering Test Satellite VII) / Kiku-7*. <https://directory.eoportal.org/web/eoportal/satellite-missions/e/ets-vii>.
- [28] Andrew Ogilvie et al. “Autonomous Satellite Servicing Using the Orbital Express Demonstration Manipulator System”. In: *Proceedings of the 9th International Symposium on Artificial Intelligence, Robotics and Automation in Space, iSAIRAS* (Jan. 2008).
- [29] David Barnhart et al. “Phoenix Program Status - 2013”. In: Sept. 2013. ISBN: 978-1-62410-239-4. DOI: [10.2514/6.2013-5341](https://doi.org/10.2514/6.2013-5341).
- [30] Kazuya Yoshida. “Achievements in space robotics”. In: *Robotics & Automation Magazine, IEEE* 16 (Jan. 2010), pp. 20–28. DOI: [10.1109/MRA.2009.934818](https://doi.org/10.1109/MRA.2009.934818).
- [31] Marco M. Castronuovo. “Active space debris removal—A preliminary mission analysis and design”. In: *Acta Astronautica* 69.9 (2011), pp. 848–859. ISSN: 0094-5765. DOI: <https://doi.org/10.1016/j.actaastro.2011.04.017>. URL: <https://www.sciencedirect.com/science/article/pii/S0094576511001287>.
- [32] Hugh Lewis. *The Growing Problem of Space Junk*. <https://themobilecentury.com/the-growing-problem-of-space-junk/>. The Mobile Century. 2015.
- [33] “Satellite Box Score”. In: *Orbital Debris Quarterly News*. Vol. 23 no. 4. NASA. November 2019. p. 10. Archived from the original on 24 December 2019. Retrieved 24 December 2019.

- [34] “UCS Satellite Database”. In: *Nuclear Weapons & Global Security*. Union of Concerned Scientists. 16 December 2019. Archived from the original on 20 December 2019. Retrieved 24 December 2019.
- [35] *Space Debris and Human Spacecraft*. https://www.nasa.gov/mission_pages/station/news/orbital_debris.html.
- [36] Donald J. Kessler and Burton G. Cour-Palais. “Collision frequency of artificial satellites: The creation of a debris belt”. In: *Journal of Geophysical Research: Space Physics* 83.A6 (1978), pp. 2637–2646. DOI: <https://doi.org/10.1029/JA083iA06p02637>. eprint: <https://agupubs.onlinelibrary.wiley.com/doi/pdf/10.1029/JA083iA06p02637>. URL: <https://agupubs.onlinelibrary.wiley.com/doi/abs/10.1029/JA083iA06p02637>.
- [37] J.-C. Liou and N.L. Johnson. “Instability of the present LEO satellite populations”. In: *Advances in Space Research* 41.7 (2008), pp. 1046–1053. ISSN: 0273-1177. DOI: <https://doi.org/10.1016/j.asr.2007.04.081>. URL: <https://www.sciencedirect.com/science/article/pii/S0273117707004097>.
- [38] J.-C. Liou and Nicholas L. Johnson. “A sensitivity study of the effectiveness of active debris removal in LEO”. In: *Acta Astronautica* 64.2 (2009), pp. 236–243. ISSN: 0094-5765. DOI: <https://doi.org/10.1016/j.actaastro.2008.07.009>. URL: <https://www.sciencedirect.com/science/article/pii/S0094576508002634>.
- [39] Kartik Kumar et al. “Agora: Mission to demonstrate technologies to actively remove Ariane rocket bodies”. In: Oct. 2015.
- [40] A. Bylard et al. “Robust capture and deorbit of rocket body debris using controllable dry adhesion”. In: *2017 IEEE Aerospace Conference*. 2017, pp. 1–9. DOI: [10.1109/AERO.2017.7943844](https://doi.org/10.1109/AERO.2017.7943844).
- [41] Jonathan Amos. *Space harpoon skewers 'orbital debris'*. <https://www.bbc.com/news/science-environment-47252304>. BBC Science. 2019.
- [42] *Orbital Debris — with Themes: Space Debris Measurements, Active Debris Removal, Sustainable Future, and First Laser Detection of Space Debris*. <https://directory.eoportal.org/web/eoportal/satellite-missions/content/-/article/orbital-debris>. eoPortal Directory/ Satellite Missions.
- [43] *The current state of space debris*. https://www.esa.int/Safety_Security/Space_Debris/The_current_state_of_space_debris. ESA/ Safety & Security/ Space Debris. 12 October 2020.
- [44] “Committee on the Peaceful Uses of Outer Space Scientific and Technical Subcommittee Fifty-sixth session”. In: *Guidelines for the Long-term Sustainability of Outer Space Activities*. 2018.

-
- [45] *e.Deorbit's robotic arm*. https://www.esa.int/ESA_Multimedia/Images/2017/01/e.Deorbit_s_robotic_arm. ESA/ Enambling & support. 18 January 2017.
- [46] *e.Deorbit will be the first-ever active debris removal mission*. https://www.esa.int/ESA_Multimedia/Images/2016/12/e.Deorbit_will_be_the_first-ever_active_debris_removal_mission2. ESA/ Enambling & support. 23 November 2016.
- [47] *From active debris removal to in-orbit servicing: the legacy of e.Deorbit*. <https://blogs.esa.int/clearspace/2018/11/26/from-active-debris-removal-to-in-orbit-servicing-the-legacy-of-e-deorbit/>. 26 November 2018.
- [48] *ESA commissions world's first space debris removal*. https://www.esa.int/Safety_Security/Clean_Space/ESA_commissions_world_s_first_space_debris_removal. 9 December 2019.
- [49] *Elecnor DEIMOS to provide the control system of the first European mission to clean space*. <https://elecnor-deimos.com/clearspace/>. 25 September 2020.
- [50] Detlef Reintsema et al. "DEOS – The German Robotics Approach to Secure and De-Orbit Malfunctioned Satellites from Low Earth Orbits". In: (2010).
- [51] *DEOS*. https://elecnor-deimos.com/clearspace/https://space.skyrocket.de/doc_sdat/deos.htm.
- [52] Alin Albu-Schäffer. "DLR's Robotic Technologies for Space Debris Mitigation and On-Orbit Servicing". In: (). Institute of Robotics and Mechatronics. URL: <https://www.unoosa.org/pdf/pres/stsc2013/2013iaf-05E.pdf>.
- [53] Jason L. Forshaw et al. "RemoveDEBRIS: An in-orbit active debris removal demonstration mission". In: *Acta Astronautica* 127 (2016), pp. 448–463. ISSN: 0094-5765. DOI: <https://doi.org/10.1016/j.actaastro.2016.06.018>. URL: <https://www.sciencedirect.com/science/article/pii/S009457651530117X>.
- [54] *RemoveDebris Mission*. <https://directory.eoportal.org/web/eoportal/satellite-missions/r/removedebris>. eoPortal Directory/ Satellite Missions.
- [55] G. S. Aglietti, B. Taylor, S. Fellowes, S. Ainley, D. Tye, C. Cox, A. Zarkesh, A. Mafficini, N. Vinkoff, K. Bashford, Thierry Salmon, Ingo Retat, Christopher Burgess, Alexander Hall, Thomas Chabot, K. Kanani, Aurelien Pisseloup, Cesar Bernal, Francois Chaumette, Alexandre Pollini and W. H. Steyn. "Remove Debris Mission: In-orbit Operations". In: *Proceedings of the 33rd Annual AIAA/USU Conference on Small Satellites* (2019). URL: <https://digitalcommons.usu.edu/smallsat/2019/all2019/153/>.

- [56] Wigbert Fehse. *Automated Rendezvous and Docking of Spacecraft*. Cambridge Aerospace Series. Cambridge University Press, 2003. DOI: [10.1017/CB09780511543388](https://doi.org/10.1017/CB09780511543388).
- [57] *RemoveDebris Mission Guidance, Navigation & Control*. <https://www.nasa.gov/smallsat-institute/sst-soa-2020/guidance-navigation-and-control>. NASA/ State of the Art of Small Spacecraft Technology.
- [58] Yaguang Yang. “Analytic LQR Design for Spacecraft Control System Based on Quaternion Model”. In: *Journal of Aerospace Engineering* 25 (July 2012), pp. 448–453. DOI: [10.1061/\(ASCE\)AS.1943-5525.0000142](https://doi.org/10.1061/(ASCE)AS.1943-5525.0000142).
- [59] James Onojo. “Design of linear quadratic regulator for the three-axis attitude control system stabilization of microsatellites”. In: (Sept. 2018).
- [60] Fu Teng et al. “Research on Attitude Control of Spacecraft Based on ADRC”. In: *Advanced Materials Research* 383-390 (Nov. 2011), pp. 358–365. DOI: [10.4028/www.scientific.net/AMR.383-390.358](https://doi.org/10.4028/www.scientific.net/AMR.383-390.358).
- [61] Chen Gao, Jianping Yuan, and Yakun Zhao. “ADRC for spacecraft attitude and position synchronization in libration point orbits”. In: *Acta Astronautica* 145 (2018), pp. 238–249. ISSN: 0094-5765. DOI: <https://doi.org/10.1016/j.actaastro.2018.01.039>. URL: <https://www.sciencedirect.com/science/article/pii/S0094576517306380>.
- [62] Ryu Funase, Hiroyuki Koizumi, Shinichi Nakasuka, Yasuhiro Kawakatsu, Yosuke Fukushima, Atsushi Tomiki, Yuta Kobayashi, Jun’ichi Nakatsuka, Makoto Mita, Daisuke Kobayashi and Taku Nonomura. “50kg-class Deep Space Exploration Technology Demonstration Micro-spacecraft PROCYON”. In: *Proceedings of the AIAA/USU Conference on Small Satellites*. Logan, Utah, USA, August 2-7, 2014, paper: SSC14-VI-3. URL: <http://digitalcommons.usu.edu/cgi/viewcontent.cgi?article=3102&context=smallsat>.
- [63] F. Landis Markley and John L. Crassidis. “Attitude Kinematics and Dynamics”. In: *Fundamentals of Spacecraft Attitude Determination and Control*. New York, NY: Springer New York, 2014, pp. 67–122. ISBN: 978-1-4939-0802-8. DOI: [10.1007/978-1-4939-0802-8_3](https://doi.org/10.1007/978-1-4939-0802-8_3). URL: https://doi.org/10.1007/978-1-4939-0802-8_3.
- [64] Giulio Avanzini. “Dispense del Corso di Dinamica e Controllo di Assetto di Satelliti”. In: *Spacecraft Attitude Dynamics and Control*. Ver. 3.0.0. 2008-09.
- [65] Mohammed Chessab Mahdi, Mohammed Al-Bermani, and Mohammed Al-Bermani. “LQR Controller for Kufasat”. In: *JOURNAL OF KUFA – PHYSICS* 6 (Jan. 2014), pp. 13–20.
- [66] Leonardo Mazzini. *Flexible Spacecraft Dynamics Control and Guidance*. Nov. 2015.

- [67] Richard M. Murray, S. Shankar Sastry, and Li Zexiang. *A Mathematical Introduction to Robotic Manipulation*. 1st. USA: CRC Press, Inc., 1994. ISBN: 0849379814.
- [68] *Revolute*. <https://www.maplesoft.com/support/help/MapleSim/view.aspx?path=componentLibrary/multibody/jointsAndMotions/Revolute>. Maplesoft/MapleSim/Component Library/Multibody/Joints and Motions/Revolute.
- [69] Y. Chen. “On the dynamics and control of manipulators with slewing and deployable links”. In: 1999.
- [70] Alam Mashiul et al. “Analytical and Experimental Study Using Output-Only Modal Testing for On-Orbit Satellite Appendages”. In: *Advances in Acoustics and Vibration* 2009 (Apr. 2009). DOI: [10.1155/2009/538731](https://doi.org/10.1155/2009/538731).
- [71] Jiawei Tao, Tao Zhang, and Yongfang Nie. “Attitude Maneuvering and Vibration Reducing Control of Flexible Spacecraft Subject to Actuator Saturation and Misalignment”. In: *Shock and Vibration* 2018 (Sept. 2018), pp. 1–16. DOI: [10.1155/2018/3129834](https://doi.org/10.1155/2018/3129834).
- [72] Caleb Henry. *Eutelsat weighs adding more Quantum satellites to fleet*. <https://spacenews.com/eutelsat-adding-two-more-quantum-satellites-to-fleet/>. Space News. 2017.
- [73] Christopher Crockett. *Japanese satellite stalls in space and won't reach its asteroids*. <https://www.sciencenews.org/blog/science-ticker/japanese-satellite-stalls-space-and-wont-reach-its-asteroids?tgt=nr>. Science News. May 2015.
- [74] Stefano Di Gennaro. “Output stabilization of flexible spacecraft with active vibration suppression”. In: *Aerospace and Electronic Systems, IEEE Transactions on* 39 (Aug. 2003), pp. 747–759. DOI: [10.1109/TAES.2003.1238733](https://doi.org/10.1109/TAES.2003.1238733).
- [75] PETER W. LIKINS and GERALD E. FLEISCHER. “Results of flexible spacecraft attitude control studies utilizing hybrid coordinates”. In: *Journal of Spacecraft and Rockets* 8.3 (1971), pp. 264–273. DOI: [10.2514/3.30258](https://doi.org/10.2514/3.30258). eprint: <https://doi.org/10.2514/3.30258>. URL: <https://doi.org/10.2514/3.30258>.
- [76] P. W. Likins. “Dynamics and Control of Flexible Space Vehicles”. In: Edizione 32, Parte 1329 di JPL technical report NASA contractor report. 1970.
- [77] Shahram Shahriari, Shahram Azadi, and Majid M. Moghaddam. “An accurate and simple model for flexible satellites for three-dimensional studies”. In: *Journal of Mechanical Science and Technology* 24 (June 2010). DOI: [10.1007/s12206-010-0329-0](https://doi.org/10.1007/s12206-010-0329-0).
- [78] Ohseop Song. *Modal Analysis of A Cantilever Plate*. 1986.

- [79] NX Nastran. *Basic Dynamic Analysis User's Guide*. Siemens Product Life-cycle Management Software. 2014. URL: https://docs.plm.automation.siemens.com/data_services/resources/nxnastran/10/help/en_US/tdocExt/pdf/basic_dynamics.pdf.
- [80] Manuel Beschi et al. "Using of the Robotic Operating System for PID control education". In: *IFAC-PapersOnLine* 48.29 (2015). IFAC Workshop on Internet Based Control Education IBCE15, pp. 87–92. ISSN: 2405-8963. DOI: <https://doi.org/10.1016/j.ifacol.2015.11.218>. URL: <https://www.sciencedirect.com/science/article/pii/S2405896315024763>.
- [81] Mark Haidekker. "The PID Controller". In: Dec. 2013, pp. 193–208. ISBN: 9780124058750. DOI: [10.1016/B978-0-12-405875-0.00013-9](https://doi.org/10.1016/B978-0-12-405875-0.00013-9).
- [82] E. Capello and F. Dabbene. *Lesson 2: Control specifications and PID control*. Dispense del corso di Dinamica e Controllo di Veicoli Spaziali. Politecnico di Torino, 2019/20.
- [83] G. Zhang et al. "Longitudinal attitude controller design for aircraft landing with disturbance using ADRC/LQR". In: *2013 IEEE International Conference on Automation Science and Engineering (CASE)*. 2013, pp. 330–335. DOI: [10.1109/CoASE.2013.6653919](https://doi.org/10.1109/CoASE.2013.6653919).
- [84] YV Wen-bin and Yan Dong. "Modeling and Simulation of an Active Disturbance Rejection Controller Based on Matlab / Simulink". In: 2015.
- [85] H. Yang et al. "Active Disturbance Rejection Attitude Control for a Dual Closed-Loop Quadrotor Under Gust Wind". In: *IEEE Transactions on Control Systems Technology* 26.4 (2018), pp. 1400–1405. DOI: [10.1109/TCST.2017.2710951](https://doi.org/10.1109/TCST.2017.2710951).
- [86] J. Han. "From PID to Active Disturbance Rejection Control". In: *IEEE Transactions on Industrial Electronics* 56.3 (2009), pp. 900–906. DOI: [10.1109/TIE.2008.2011621](https://doi.org/10.1109/TIE.2008.2011621).
- [87] Y. Xie et al. "Design and Implementation of an Efficient Tracking Differentiator". In: *IEEE Access* 7 (2019), pp. 101941–101949. DOI: [10.1109/ACCESS.2019.2930963](https://doi.org/10.1109/ACCESS.2019.2930963).
- [88] C. Li, T. Cai, and Z. Han. "Disturbance prediction based active disturbance rejection control approach". In: *2016 35th Chinese Control Conference (CCC)*. 2016, pp. 5896–5900. DOI: [10.1109/ChiCC.2016.7554281](https://doi.org/10.1109/ChiCC.2016.7554281).
- [89] Suiyuan Shen and Jinfu Xu. "Attitude Active Disturbance Rejection Control of the Quadrotor and Its Parameter Tuning". In: *Hindawi* (2020). DOI: [10.1155/2020/8876177](https://doi.org/10.1155/2020/8876177).

BIBLIOGRAPHY

- [90] Lucy Jackson et al. “Downsizing an orbital space robot: A dynamic system based evaluation”. In: *Advances in Space Research* 65.10 (2020), pp. 2247–2262. ISSN: 0273-1177. DOI: <https://doi.org/10.1016/j.asr.2020.03.004>. URL: <https://www.sciencedirect.com/science/article/pii/S0273117720301435>.
- [91] Satoshi Ikari et al. “Attitude Determination and Control System for the PROCYON Micro-Spacecraft”. In: *TRANSACTIONS OF THE JAPAN SOCIETY FOR AERONAUTICAL AND SPACE SCIENCES* 60 (May 2017), pp. 181–191. DOI: [10.2322/tjsass.60.181](https://doi.org/10.2322/tjsass.60.181).
- [92] Takahiro Ito et al. “Reliable and Robust Implementation of Attitude Determination and Control Subsystem and Initial Flight Operation Result of 50 kg-class Interplanetary Spacecraft PROCYON”. In: Oct. 2015.